POLITECNICO
MILANO 1863

SCUOLA DI INGEGNERIA INDUSTRIALE
E DELL'INFORMAZIONE

CFD analysis of a solar powered bayonet-tube reformer processing biogas

Tesi di Laurea Magistrale in
Energy Engineering - Ingegneria Energetica

Author: **Stefano Luca Monti**

Student ID: 969553
Advisor: Prof. Matteo Maestri
Co-advisors:
Academic Year: 2022-23

Abstract

The introduction of spider baffles and the effectiveness of the turbulence generated in terms of convective heat exchange in a bayonet-tube reforming reactor, connected to a solar tower, fed with biogas for syngas production, was studied in this thesis work. CFD simulations using ANSYS Fluent were carried out in order to evaluate the increase in convective heat transfer considering three different reactor geometries, with variable baffle size and smooth tube. The importance of convective versus radiative heat transfer and the effect of introducing baffles on reactant conversion and the quality of the syngas produced were analysed. **Keywords:** syngas,turbulence,reforming,biogas

Abstract in lingua italiana

L'introduzione di spider baffles e l'efficacia della turbolenza generata in termini di scambio termico convettivo in un reattore di reforming con configurazione a baionetta, collegato a una torre solare, alimentato a biogas per produzione di syngas, è stata studiata nel presente lavoro di tesi. Simulazioni CFD usando ANSYS Fluent sono state svolte con lo scopo di valutare l'incremento dello scambio termico convettivo considerando tre differenti geometrie del reattore, con dimensione variabile dei baffles e a tubo liscio. L'importanza dello scambio termico convettivo rispetto allo scambio termico radiativo e l'effetto dell'introduzione dei baffles sulla conversione dei reagenti e la qualità del syngas prodotto è stata analizzata. **Parole chiave:** gas di sintesi,turbolenza,reforming,biogas

Contents

Introduction

Greenhouse gases (GHGs) emissions related to fossil fuel combustion, either in the transport sector or in the industrial one, is a problem to deal with in order to control and reduce global warming. The main concern is related to fossil fuel combustion, because a quantity of carbon, stored in the ground, is in this way transformed in carbon dioxide (CO_2) causing a net positive release of it in the environment; it is important to underline that CO_2 is not a pollutant per se, in the sense that it is not toxic for humans, but it is a cause of the greenhouse effect and an increasing concentration of CO_2 in the environment is strictly related to climate change. In order to meet the Paris Agreement climate target of limiting the global temperature rise within 2 °C, an important amount of GHGs emissions should be avoided. In terms of CO_2 global emissions in the atmosphere, a decrease of 45% should be reached by 2030 to limit the global warming to 1.5 °C and after that, a net zero emission should be achieved by 2050. Different paths can be followed to achieve this objective, in all the sectors that are related to relevant GHGs emissions, starting from transportation to industrial plants. Utilisation of biomass is of key importance for global decarbonization because it allows to produce both fuels and chemicals in carbon negative process. From biomass is possible to produce syngas an important energy carrier of increasing importance, which is a gaseous mixture containing high quantity of hydrogen (H_2) and/or carbon monoxide (CO). Syngas is of great interest because it is an intermediate product that can be used as a way to produce pure hydrogen, that could be an important energy carrier in the next future, due to the possibility to use it as fuel for Internal Combustion Engine (ICE) or as working fluid in stationary power plants to produce energy. It is then possible to use syngas in a Fischer-Tropsh (FT) process to transform it in liquid synthetic fuel, for transportation, having fuels more similar to the standard fossil ones used for these applications; this last path is crucial to decarbonize the transportation sector. This thesis work has the aim of assessing through a CFD analysis on ANSYS Fluent, the performance, in terms of heat transfer and conversion, of a bayonet-tube biogas reformer, in particular highlighting the effects of the introduction of baffles, in order to enhance the heat transfer. In the first chapter, an overview on the state of the art of syngas production through methane reforming will be performed, focusing on

both the developed processes and the new technologies. In the second chapter a particular bayonet-tube biogas reformer will be presented, clarifying the process in which it takes part and its geometry. In the third chapter an overview on the CFD models, available in ANSYS Fluent, that have been used to carry out the simulations, will be deeply discussed. In the fourth chapter, the setup of the CFD simulations will be shown, explaining the reasons behind the different choices. In the fifth chapter, the results of the simulations will be shown and a comparison between the different geometries considered will be presented. Finally, in the last chapter the conclusions of this work will be summarized while considering possible next steps for the development of this reformer.

1 | State of the art

1.1. Synthesis gas role in decarbonization

Synthesis gas, also known as syngas, is a gaseous mixture primarily composed of carbon monoxide (CO) and hydrogen (H_2) in varying proportions. Other components such as carbon dioxide (CO_2), water (H_2O), and nitrogen (N_2) may also be present. Syngas is currently of significant interest because it serves as a versatile building block for various chemical products, including methanol (MeOH) and dimethyl ether (DME). Furthermore, it represents an important intermediate product in both the energy and fuel production industries [1]. Syngas can be produced from either solid feedstocks like coal or gaseous ones such as natural gas or biogas. It is a crucial component in hydrogen production from fossil fuels, particularly from natural gas. When combined with carbon capture and storage (CCS) technology, syngas production can result in negligible CO_2 emissions, making it an attractive option for achieving a greener future [2]. Syngas is also a crucial intermediate product in the transportation sector, where it can be converted into synthetic fuels via the Fischer-Tropsch process. This process can produce fuels that are identical to fossil fuels while being environmentally sustainable [3]. The H_2/CO molar ratio is an important parameter to consider when using syngas, as it determines the downstream applications. For example, an efficient Fischer-Tropsch process requires a H_2/CO ratio between 1 and 2.5 [4]. The development of syngas production technologies is essential in the energy sector to increase efficiency and to make laboratory-scale processes feasible in an industrial setting. Among the various methods to produce syngas, the steam reforming process, which uses natural gas as a feedstock, is the most widely adopted for hydrogen production. However, much effort is being put into developing pathways that result in low CO_2 emissions while still producing the desired product.

1.2. Methane reforming processes

The majority of the world's syngas production is reliant on methane reforming processes. The composition of the resulting syngas can vary significantly depending on the feedstock

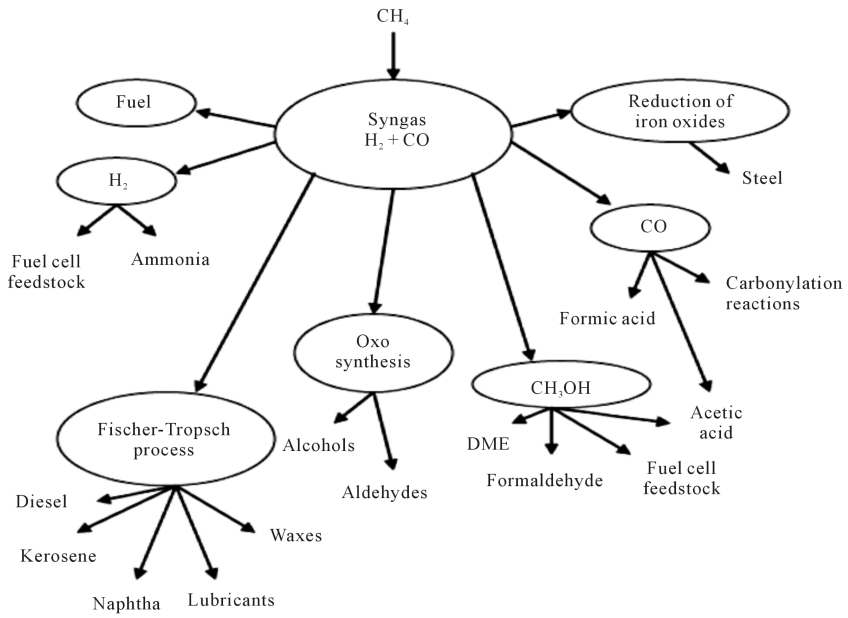

Figure 1.1: Syngas as intermediate product

and process used, resulting in different ratios of hydrogen to carbon monoxide (H_2/CO). It is important to note that methane reforming processes produce significant amounts of CO_2 as a byproduct. The quantity of CO_2 produced per mole of syngas is dependent on the technology and feedstock used. Additionally, in non-autothermal processes, a significant amount of heat must be provided to facilitate syngas production. The CO_2 emissions associated with the combustion required for this heat must also be taken into account when calculating the overall CO_2 emissions from the reforming process. As a result, natural gas is the preferred feedstock due to its high hydrogen to carbon ratio. Several reliable and established reforming technologies currently available on the market utilize natural gas as the main feedstock:

- Steam methane reforming (SMR)
- Partial oxidation (POX)
- Catalytic partial oxidation (CPOX)
- Auto thermal reforming (ATR)

However, there are ongoing research efforts focused on developing innovative reforming concepts, such as:

- Dry reforming (DR)
- Bi-reforming (BR)

- Tri-reforming (TR)

1.2.1. Steam methane reforming (SMR)

Steam reforming of methane (SMR) has been introduced in 1924. It is the most technologically developed process adopted to produce syngas and in particular pure hydrogen, due to the high H_2 molar fraction in the synthesis gas. The inlet feed of the SMR reactor accounts for natural gas and superheated steam. The reactions considered in the process are multiple, as follows:

$$CH_4 + H_2O \rightleftarrows CO + 3\,H_2 \qquad \Delta H^o_{298} = 206\frac{kJ}{kmol} \tag{1.1}$$

$$CO + H_2O \rightleftarrows CO_2 + H_2 \qquad \Delta H^o_{298} = -41\frac{kJ}{kmol} \tag{1.2}$$

$$2\,CO \rightleftarrows CO_2 + C \qquad \Delta H^o_{298} = -172\frac{kJ}{kmol} \tag{1.3}$$

$$CH_4 \rightleftarrows C + 2\,H_2 \qquad \Delta H^o_{298} = 75\frac{kJ}{kmol} \tag{1.4}$$

$$C + H_2O \rightleftarrows CO + H_2 \qquad \Delta H^o_{298} = 131\frac{kJ}{kmol} \tag{1.5}$$

The reforming process requests an high quantity of heat in order to make the reaction proceed towards the products and this is mainly due to the strong endothermic nature of the steam reforming reaction (eq. 1.1). Reaction 1.2 is the water gas shift (WGS) reaction which is fundamental in order to achieve the desired amount of CO and H_2. Being the steam reforming reaction endothermic, it is favoured at high temperatures. In the steam reforming reaction, the number of moles of the products is higher with respect to the number of moles of the reactants and for this reason it is favoured at low pressures. On the other hand increasing the pressure of the process is beneficial in terms of dimensions of the reactor and, for some downtream applications, having the products in pressure could be preferred. Typically the temperature operating range is between 800 and 900 °C while pressure is in the range of 30 bar [5]. In order to achieve high methane conversion, temperature at the reformer exit is kept between 870 and 920 °C [6]. A key aspect of a reforming process is related to the heat source adopted to feed the reactor, because this is, for all the technologies presented, crucial in order to evaluate the CO_2 emissions of the whole process. A mixture of natural gas and potential off-gases from the synthesis is typically combusted to supply the necessary heat in the standard steam methane reforming process. Nearly 50% of the heat supplied by burning the fuel is lost [7]. The typical configuration of SMR is called Fired Tubular Reformer (FTR) and it consists of a furnace containing more than 100 tubes, with a length between

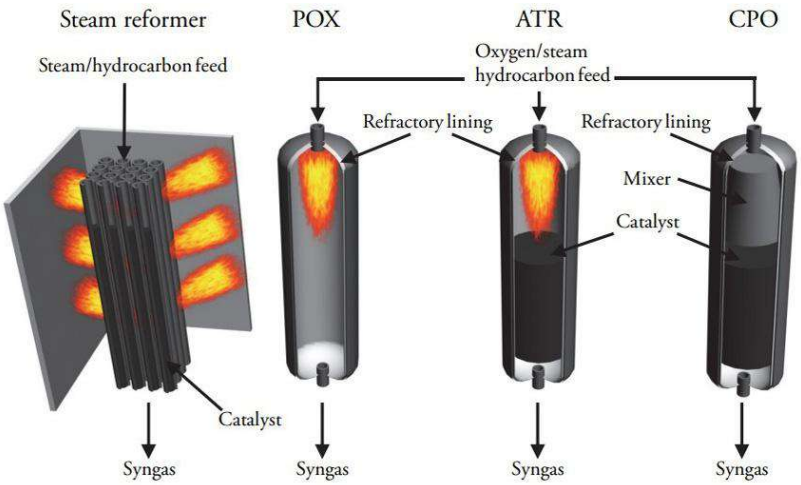

Figure 1.2: Most common reformer technologies

10 and 14 m. Therefore reformers are quite bulky and can take up 1140 m^3 just to achieve a methane conversion of 75% [8]. Most SMR units consist of two sections: a radiant section where reforming reactions occur and a convective section where heat is recovered from high temperature product gases. The recovered heat is used for preheating reactant feeds and generating superheated steam. The steam methane reforming process is a catalytic process, which means that a catalyst is necessary in order to reach the desired conversion of methane, the correct yield of the products and to allow the reaction to activate at lower temperatures. Noble metals such as Rh and Ru have the highest activity for steam reforming. However, due to the high price of these metals, they are not used in conventional steam reformers. The preferred choice in industrial steam reforming catalysts is Nickel (Ni), which has good steam reforming activity and moderate price [9]. Nickel (Ni) is supported on an oxide carrier, typically Al_2O_3, ZrO_2, $MgAl_2O_4$, $CaO(Al_2O_3)$ and MgO [10]. The adoption of Nickel as catalyst promote the reactions 1.3 and 1.4 that are dangerous because solid carbon is produced. Solid carbon deposition is the main cause of catalyst deactivation. Usually the catalyst is present into the reforming tubes as in a fixed or fluidized bed configuration. Both fixed and fluidized beds present good selectivity and yields for H_2 production [11]. Fixed bed reactors are basic reactors made up of packed solid catalyst particles. However, they have limitations due to their low thermal conductivity and limited surface area for the catalyst inside the reactor. On the other hand, fluidized bed reactors use small catalyst particles that act like a fluid when mixed with the reactant gas flow. This technology overcomes the issues faced by fixed bed reactors by improving mass and heat transfer and reducing temperature

differences inside the reactor. This method allows for better mixing of the reactant fluid and catalyst, which creates a larger surface area for the reaction to take place [12]. An important inlet parameter of the SMR process is the S/C ratio, which refers to the ratio between steam and carbon or H_2O and CH_4, which is the same. Large S/C ratio means high quantity of steam with respect to carbon. In this conditions high conversion of methane can be reached but producing steam at high temperature and pressure is costly from an economic and energy related point of view. Carbon deposition on the catalyst can become a problem in steam reformers, especially for low S/C ratios (economically desirable) and with feedstocks containing heavier hydrocarbons with respect to CH_4. For this reason the S/C ratio needs to be maintained between 2.5 and 3 in order to avoid catalyst deactivation due to carbon deposition. The carbon can cause sintering and can also deposit in the catalyst pores, which will reduce catalytic activity and eventually disintegrate the catalyst pellets to powder. Two processes are present upstream and downstream the FTR reactor, in order to complete the SMR processes. Upstream the FTR a pre-reformer is adopted. This unit is necessary because allows to break the heaviest hydrocarbons (C_2-C_5) preparing the inlet feed of the FTR as a mixture of CH_4, CO, CO_2, H_2O and H_2 [13]. The Pre-reforming process is of key importance, because having only carbon in the form of CH_4 allows to reach higher temperature at the inlet of the FTR resulting in a more compact and efficient section [14]. Downstream the FTR typically two sections of water gas shift (WGS) reactors are present in order to transform the CO in H_2, allowing to produce H_2 rich syngas for pure hydrogen production. Steam methane reformer is the leader technology for th production of pure H_2. This is possible because the syngas obtained is characterized by a H_2/CO ratio of 3. It is the most widely used method for producing syngas from natural gas, accounting for 50% of global natural gas conversion processes for hydrogen production. In the United States, this percentage reaches 90% [15].

1.2.2. Adiabatic oxidative reforming

Adiabatic oxidative reforming is a family of processes in which the heat required for reforming reactions is generated by internally combusting a portion of the reactants. This differs from the FTR technology, which relies on external sources for heat feeding. In steam reforming, the composition of the resulting synthesis gas is determined solely by the steam reforming reaction and water gas shift reaction. However, adiabatic oxidative reforming introduces additional reactions. The overall reaction is adiabatic, which means that there is no exchange of heat with the surroundings, except for a small amount of heat loss. To produce synthesis gas, a sub-stoichiometric amount of oxidant is added, ensuring

that all oxygen is consumed since it is the limiting reactant.

Partial oxidation (POX)

The partial oxidation process has been developed more than 100 years ago. The aim of the technology is syngas production, adopting hydrocarbons, steam and pure oxygen as inlet feed. The process is able to convert even heavy hydrocarbons, such as coal or solid biomass. The key reactions involved in this process [16], other than the steam reforming reaction (eq. 1.1) and the water gas shift (eq.1.2), are:

$$CH_4 + \frac{1}{2}O_2 \longrightarrow CO + 2\,H_2 \qquad \Delta H^o_{298} = -36\frac{kJ}{kmol} \tag{1.6}$$

$$CH_4 + O_2 \longrightarrow CO + H_2 + H_2O \qquad \Delta H^o_{298} = -278\frac{kJ}{kmol} \tag{1.7}$$

$$CH_4 + \frac{3}{2}O_2 \longrightarrow CO + 2\,H_2O \qquad \Delta H^o_{298} = -519\frac{kJ}{kmol} \tag{1.8}$$

$$CH_4 + 2\,O_2 \longrightarrow CO_2 + 2\,H_2O \qquad \Delta H^o_{298} = -802\frac{kJ}{kmol} \tag{1.9}$$

$$CH_4 + 2\,H_2O \longrightarrow CO_2 + 4\,H_2 \qquad \Delta H^o_{298} = -165\frac{kJ}{kmol} \tag{1.10}$$

$$CH_4 + CO_2 \longrightarrow 2\,CO + 2\,H_2 \qquad \Delta H^o_{298} = 247\frac{kJ}{kmol} \tag{1.11}$$

Reactions (1.1), (1.2), (1.6) and (1.11) are responsible for the H_2 and CO production and are mostly endothermic. Reactions (1.7), (1.8), (1.9) and (1.10) are the partial and complete oxidation reactions of methane and are highly exothermic. The heat necessary for the reforming reactions is produced by the oxidation reactions and there is no need for external heat, which makes the system autothermal [17]. The operating conditions inside the reactor are severe both in terms of temperature and pressure [18]. The reactor operates in a temperature range between 1150 - 1500 °C, depending on the inlet feed. At the inlet the oxygen-to-fuel ratio is lower with respect to the stoichiometric and, for this reason, high temperatures are reached inside the reformer. The system can work in a large range of pressure from 25 - 80 bar. The POX reactor is more compact with respect to the SMR reactor but it is less efficient. The configuration of the technology is divided into two parts: a first part in which methane, oxygen and steam, in variable quantities, undergo the oxidation and reforming reactions and a second part in which an heat exchanger allow to recover the heat from the products, to minimize the thermal losses. In the first part, due to the presence of CH_4 and O_2 in high quantities there is the risk of explosion [19]. An high S/C ratio enhance the SR and WGS reactions allowing to reach high production of $H2$ but it is detrimental because determines a larger soot formation in the reformer[20].

Due to the high operating temperature and pressures there is no need for the catalyst [21]. The POX technology is capable of producing a syngas characterized by an H_2/CO equal to 1.7 - 1.8, which makes it feasible both for pure hydrogen or synthetic fuel production. The methane conversion of the process stands between 70 - 80 %. On the other hand, the yield of H_2 is much lower with respect to the SMR, reaching values of 40 - 50 %. The most important drawback of the POX technology is related to the necessity of having pure O_2, which makes necessary to have an Air Separation Unit (ASU). For this reason the POX can be adopted only for large scale applications.

Catalytic partial oxidation (CPOX)

Catalytic partial oxidation (CPOX) is a technology similar to the POX in which the key difference is related to the presence of the catalyst. The inlet feed of the reactor contains hydrocarbons and pure oxygen. Both liquid and gaseous hydrocarbons can be converted in this kind of reformer. No steam addiction is required. The sulphur content of the feed, while referring to natural gas, needs to remain in low concentrations (lower than 60 ppm) in order to avoid catalyst poisoning. Pure O_2 is required as inlet feed, because using air a too large quantity of N_2 would be present in the synthesis gas produced, which makes necessary to adopt downstream components of larger dimensions and cost, having the same quantity of the desired products (H_2 and CO). The reactions that are carried out in a CPOX reformer are partial and complete oxidation of CH_4 and the reforming reactions (equations 1.6-1.10), the WGS reaction (eq.1.2), and the following reactions:

$$H_2 + \frac{1}{2}O_2 \longrightarrow H_2O \tag{1.12}$$

$$CO + \frac{1}{2}O_2 \longrightarrow CO_2 \tag{1.13}$$

$$2\,CO \longrightarrow CO_2 + C \tag{1.14}$$

Reactions 1.8 and 1.9 are the complete oxidation of hydrogen (H_2) and carbon monoxide (CO) and activate at low temperatures. These reactions need to be avoided as much as possible because H_2 and CO are the desired products. The preferred reaction to be obtained is reaction 1.3 because allows to directly obtain the desired products, with a low thermal energy required. All the reactions happen in heterogeneous phase in presence of the catalyst. Due to the adoption of the catalyst the operating temperatures and pressures are lower with respect to POX. Theoretically the temperature inside the reformer can vary between 700 and 1000 °C. It has been shown that for temperatures lower than 900 °C, the complete oxidation of H_2 and CO is enhanced, so in practice the temperature needs to remain higher than the above mentioned threshold [22]. The reformer is divided in

two parts. In the first part the feed is mixed by using a mixer. In the second section the catalyst bed is present and there all the reactions are carried out. In particular in the first *mm* of the catalytic bed, the oxidation reactions are carried out, followed by the reforming reactions. In the first part of the catalyst bed, due to the highly exothermic oxidation reactions, the temperature reaches peaks of 1100 °C [23]. In order to avoid too high temperatures in the inlet feed upstream the catalytic bed, a thermal shield is often adopted. This precaution is taken in order to avoid the autoignition of the CH_4/O_2 mixture, which has lower autoignition temperatures and pressure with respect to the CH_4/air mixture. In the CPOX reformer no burners are present and the combustion reactions are carried out chemically, thanks to the catalyst, while no flames are developed. The heat required by the endothermic reforming reactions is available thanks to the combustion reactions. For this reason, after the high temperature in the first *mm* of the catalyst bed, the temperature drops down due to the endothermic reactions. The catalysts adopted are transition metals, Ni and Co, supported on oxides (AlO_3, CaO, SiO_2, CeO_2) or noble metals, mostly Ir, Pd, Pt and Rh. Noble metals (Ir, Pd, Pt, Rh) are more attractive because they present a higher catalytic activity, can operate at lower temperatures, and are less susceptible to be deactivated [24]. On the other hand, noble metals are more costly. The catalysts are present in the reformer are in the form of pellets, monoliths and foams. The energy required by the reforming reaction is lower in CPOX with respect to POX due to the presence of the catalyst[25]. The CPOX technology allows to reach H_2/CO similar to 2, which is an high value, suitable for pure hydrogen production. The CH_4 conversion and selectivity to CO and H_2 are in the order of 90% [26]. The adoption of Ni based catalyst provides higher H_2 yield. The operating conditions of CPOX allows to couple it with fuel cells [27].

Autothermal reforming (ATR)

Autothermal reforming (ATR) has been developed between 1930 and 1950. Despite being a quite old process, only a few commercial plant are available [28]. The reactions that occur in the ATR process are the SR, the WGS reactions and the partial and complete oxidations of methane, hydrogen and carbon monoxide. The methane reactions of combustion are highly exothermic and are sufficient to provide to the system the heat necessary in order to carry out the reforming reactions headed to syngas production. The inlet feed of the ATR comprises oxygen (O_2), necessary for the oxidation of methane. In particular, the process requires air enriched with oxygen, or, if the aim is pure H_2 production, pure O_2 as inlet feed, in order to avoid a too large quantity of nitrogen (N_2) in the produced syngas. In fact it would be necessary to remove it downstream and it would

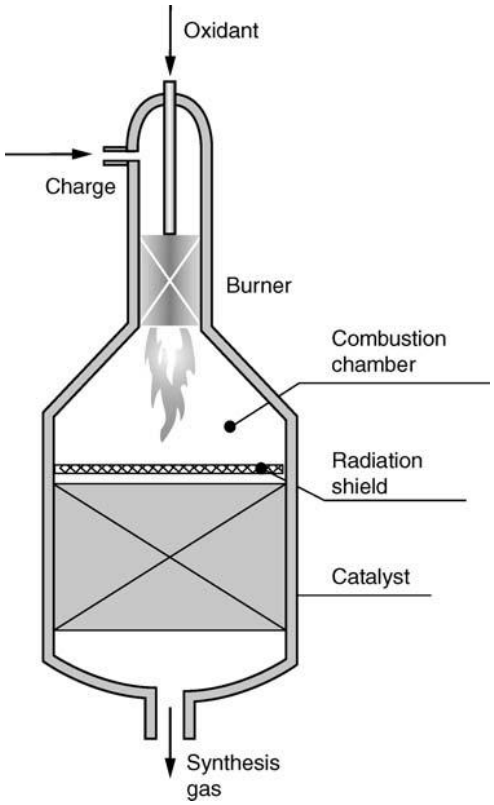

Figure 1.3: Autothermal reformer schematization [6]

strongly increase the total volumetric flow rate of the products with respect to the effective quantity of both H_2 and CO[29]. As shown in figure 1.3, the ATR configuration can be divided in three zones. In the first part a burner is present which allows for the mixing of the inlet feed (natural gas, oxygen and steam) and the beginning of combustion. In the combustion chamber the partial and complete oxidations of methane are carried out. It is important to underline that O_2 is supplied in sub-stoichiometric quantity, because an important fraction of the inlet methane needs to take part in the reforming reactions. In particular O_2/CH_4 is between 0.55 and 0.6. In the last part, in the presence of a catalyst, the reforming reactions occur. The operating conditions of the reactor are less severe. The temperature is function both of the steam-to-carbon ratio and the oxygen-to-carbon ratio. Typically high temperatures are reached in the combustion chamber, in the order of 1100 - 1300 °C, while lower temperatures are measured at the outlet, between 900 and 1000 °C [10]. The catalysts adopted in the ATR process are both transition metals and noble metals (Pt, Pd, Rh, Ru). In particular Ni-based catalyst supported on oxides, like Al_2O_3, are used. The process typically is able to produce a syngas characterized by H_2/CO equal to 2. On the other hand, the H_2/CO of the produced syngas is dependent on the H_2O/O_2 of the feed, because it modifies the energy demand of the ATR [30]. Hence, by varying the composition of the feed it is possible to obtain a syngas more suitable

for synthetic fuels production, for example. A problem that needs to be addressed in the ATR technology is the soot formation due to the combustion reactions. In order to inhibit soot formation is necessary to design correctly the burner, ensure a sufficient H_2O/CH_4 ratio and considering a catalyst which is active in converting the soot precursors. The main limitation of the ATR process is related to the need of pure O_2. Pure O_2 has to be produced in an ASU which makes the technology economically favourable only for large scales, in the order of 250′000 $\frac{Nm^3}{h}$ of H_2. A techno-economic study demonstrate the feasibility of a small scale ATR process, which uses air, adopting biogas as feedstock. The considered plant is able to produce 100 $\frac{Nm^3}{h}$ of H_2, in a process that, by the adoption of biogas, reaches the net-zero emissions target [31].

1.2.3. Dry methane reforming (DMR)

In contrast with respect to the SMR, POX, ATR and CPOX reformers presented in the last sections, Dry Reforming of methane (DMR) is not a commercial technology yet. The key interesting aspect of the DR process is related to the possibility to use both CH_4 and CO_2 in order to produce syngas. The process is catalytic and a number of different reactions can take place . The main reaction is the dry reforming reaction (eq. 1.11). This reaction is more endothermic than the steam reforming reaction (eq. 1.1) and this is the reason for which the DR process is favoured by higher temperatures with respect to the SMR process. In particular the operating temperatures of the DR are above 900 °C, while the operating pressure is low because the DR reaction involves an increasing in the number of moles. A study has been conducted on the thermodynamic equilibrium of CH4 DR under varying temperatures and pressures. The results showed that the conversion of CH4 increased as the reaction temperature rose, particularly within the range of 400 - 800 °C. This was accompanied by a significant increase in H_2 production within the same temperature range. At temperatures above 700 °C, the H_2/CO ratio could surpass 1. Furthermore, at temperatures exceeding 800 °C, complete conversion of CH_4 could theoretically be achieved [32]. The high temperatures characteristic of the DR process allow to have predominant production of CO and H_2 but strongly enhance the deactivation of the catalyst [33]. Catalyst deactivation is mostly related to the Boudouard reaction (eq.1.3) and the methane decomposition (eq.1.4) which allow the coke formation, which is enhanced by the low steam-to-carbon ratio of the process. As in the other reforming technologies, the possible catalysts are transition metals (Ni, Co, Cu, Fe) and noble metals (Pt, Pd, Rh). Noble metals are the catalysts that show the highest activity but their cost is 100 times grater with respect to Nickel-based catalysts. Between the transition metals, Nickel-based catalyst are the most studied for DR processes [34]. Bi-metallic catalyst,

transition metal with a small amount of noble metal, could represent a future solution to deactivation. A key aspect of the DMR process is related to the characteristics of the syngas produced. The syngas produced by the SMR process presents an high H_2/CO ratio which is perfect for pure H_2 production but not feasible for synthetic fuels production through Fischer-Tropsch process, where the formation of long chain hydrocarbons is suppressed by the high concentration of H_2 [35]. In contrast the DR process generates a low H_2/CO synthesis gas which is perfect for FT process headed to synthetic fuels production [36]. In general the H_2/CO is around 1. This is related to the important effect that the reverse water gas shift reaction has on the process.

$$CO_2 + H_2 \rightleftharpoons CO + H_2O \qquad \Delta H^o_{298} = 41.2\frac{kJ}{kmol} \tag{1.15}$$

Reaction (eq. 1.18) is the reverse reaction of WGS. Due to the higher concentration of CO_2 with respect to H_2O the reaction proceeds towards the CO formation and, in particular, if the H_2/CO is increasing over 1, the reaction is activated and returns the ratio to unity. The development of both DMR and RWGS reactions is such that the conversion of CO_2 is higher with respect to the conversion of the CH_4 and the H_2/CO ratio decreases [37]. The endothermic nature of the DR makes it similar to the SMR, in fact both processes need an external heat feeding, in contrast with the POX, ATR and CPOX technologies, where the process is autothermal, in the sense that the endothermic reactions are promoted and allowed by the development of combustion reactions. Considering the kind of the feed, it is important to underline that using natural gas is possible but difficult, because a stream rich of CO_2 is needed. This stream could be obtained by coupling DR with a fuel cell (FC) or by using a carbon capture and storage (CCS) system. Another, more interesting path is represented by the adoption of biogas as feed. Biogas can be obtained from various feedstocks and pre-processed with different technologies, such as anaerobic digestion. For this reason biogas composition is strongly variable depending on the refining process and on the feedstock, which makes difficult to have a standardized process. On the other hand, biogas naturally contains important concentrations of CH_4 and CO_2 which are the main reactants of the process. Usually biogas is characterized by CH_4/CO_2 between 1 and 1.5. Typically biogas shows fractions of sulphuric acid, which is dangerous even at low concentrations. The biogas need to be pre-treated before undergoing the DR because the H_2S is detrimental for the process, making the conversions of both CH_4 and CO_2 strongly decreasing [38]. Almost all the research on DMR with biogas are performed in laboratory scales and by using a fictitious biogas as feedstock. A research has shown that it is theoretically possible to integrate an anaerobic digestion plant, for biogas production, with a DR process in order to produce 8.1 $\frac{kg}{h}$ of H_2 [39].

1.2.4. Combined methane reforming

The impact of energy consumption and coke formation in the DR process is an important limitation to the industrial development of the process, both in small and large scales. For example in order to thermally feed the reactions occurring inside the tubes in the FTR, a large quantity of hydrocarbons needs to be burned, which results in high CO_2 emissions. For which regards the DR technology, more energy is required to produce the syngas, being the reaction more endothermic. This results in an higher CO_2 emission per quantity of syngas produced. In order to overcome the problems related to DMR process, the injection of H_2O and/or O_2 is interesting. In the next two sections bi-reforming and tri-reforming of methane will be presented. These technologies are under research but are attractive from different perspectives.

Bi-reforming (BRM)

The bi-reforming of methane (BRM) consists in coupling the dry reforming reaction (eq. 1.12) with the steam reforming reaction (eq. 1.1). In this way it is possible to convert both CH_4 and CO_2 while having a process that is slightly less endothermic with respect to the DR process. The main reaction considered in BRM is:

$$3\,CH_4 + 2\,H_2O + CO_2 \rightleftarrows 4\,CO + 8\,H_2 \qquad \Delta H^o_{298} = 659\frac{kJ}{kmol} \tag{1.16}$$

The above described reaction is a linear combination of the steam and dry reforming reactions. It is possible to notice that is more endothermic with respect to the steam and dry reforming reactions considered singularly but the number of moles of syngas produced is higher, which results in lower energy requested for a single mole of syngas with respect to the dry reforming reaction. The introduction of H_2O has two beneficial effects on the process. The first one is related to a reduction of the coke formation, that is decreased by the presence of H_2O [40]. An operating temperature in the order of 900 °C reduces coke formation. The second beneficial effect is related to the syngas quality. By properly modifying the H_2O/CO_2 ratio in the feed it is possible to control the H_2/CO of the process. In particular the syngas produced shows a H_2/CO ratio of 2, which is good both for undergoing the FT process or methanol production [41]. The catalysts adopted are transition metals (Ni,Co) or noble metals. NiO/MgO and CoO/MgO are the preferred one in order to further decrease the coke formation, enhance the selectivity and increase the reactants conversion [42]. The adoption of biogas as feed is interesting in order to reduce the environmental impact of the process, potentially making it a net-zero CO_2 emission process depending on the heat source. The drawbacks of using biogas are

related to its impurities which can be detrimental for the process if not refined correctly [43].

Tri-reforming (TRM)

The Tri-reforming of methane (TRM) process relies on the idea of injecting H_2O and O_2 in a DRM process, in order to realize a set of reactions that make the whole process thermally neutral [44]. The reaction that defines the process is the following one: This unique reaction contains the three main reactions that describe the SMR, CPOX and DRM processes. TRM is in fact a combination of the above mentioned processes. As it is possible to see from equation 1.17, the TRM process is slightly endothermic, because the hig endothermic nature of both SMR and DMR processes is balanced by the combustion reactions of CPOX process. This is the most important advantage of the TRM process with respect to SMR and DMR. This technology is capable of producing syngas at a temperature between 700 and 900 °C and at atmospheric pressure [45]. Low pressures are favourable for the process but typically, producing the syngas at high pressures is necessary depending on the downstream applications. The syngas produced is characterized by H_2/CO between 1.7 and 2.7. The range of variation is such large because it is possible to modify it by varying the relative quantities of the reactants (CH_4, CO_2, O_2, H_2O) [46]. The catalysts adopted in this technology are Ni-based type. This catalyst shows high activity both with natural gas and biogas [47]. Coke formation is a problem this technology but steam addition is adopted in order to reduce this mechanism [48]. Tri-reforming of methane reactors are not commercially available but many studies have been conducted on laboratory-scale facilities and, through the development of suitable catalysts, the technology could become reliable [49].

1.3. Heat exchange reformers (HER)

For small scale SMR plants, FTR has been replaced by newer designs with more efficient heat transfer. The ability of the radiative-type reformer of converting the heat input, obtained by fossil fuel combustion, to heat available for the reforming reaction is quite low (around 50%). To solve the need of increasing the heat transfer properties of the reforming processes, heat exchange reformers have been taken into consideration. In this reformers configuration, the heat for the reactions is provided by convection rather than radiation, by adopting a gas flow as a medium. Theoretically, the heat can be transferred by using flue gases, process gases or in general any gas available, being this gas only an heat transfer medium. When considering only the heat and mass balance on the flow

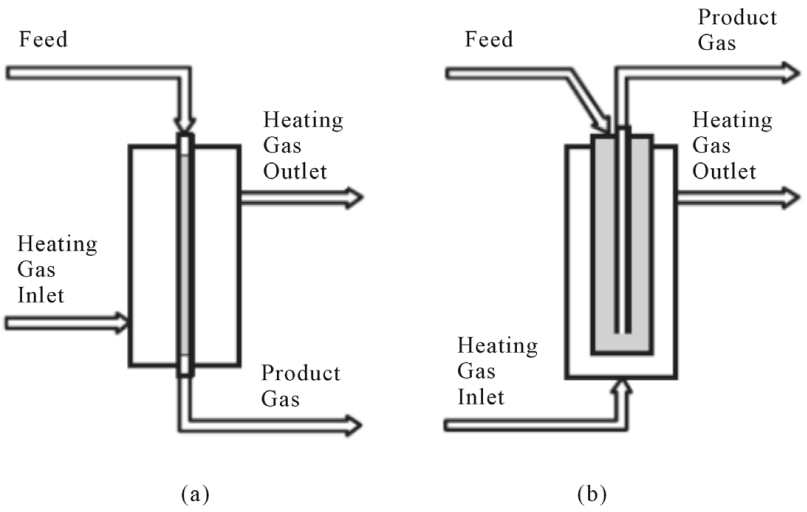

Figure 1.4: Heat exchange reformer configurations [10]

that undergoes reactions, there is no difference between heat exchange reforming and fired tubular reforming, where heat transfer is mainly by radiation. This implies that all process designs utilizing heat exchange reforming can have alternatives where the function of the heat exchange reformer is carried out in a fired reformer. The process designs only vary in the quantity of latent heat in flue gas and/or process gas and in how this heat is utilized. The HER configuration can be adopted theoretically in every reforming process in which the heat supply is decoupled by the reaction side (SMR, DRM and BRM). Two different HER configurations, shown in figure 1.4, have been proposed. In these two configurations the heat transfer medium is decoupled by the reaction side, so it is possible to choose it without any constraint. In general the heat can be provided to the heat transfer fluid through combustion. Yu et al. [50] developed a mathematical model, which was validated with experimental data, for steam methane reforming (SMR) in a heat exchanger-type steam reformer. In this process, the reaction gas mixture is introduced into the reformer through a catalytic tube from the top, while hot flue gases flow from the bottom to the top in a counter-flow arrangement. The reformer consists of 168 tubes, each with an effective length of 12.3 meters. The reaction mixture feed temperature is 439 °C, while the inlet and outlet temperatures of the hot flue gas are 955 °C and 515 °C, respectively. Consequently, there exists a steep temperature gradient between the heat source, the tube, and the reaction gas, which requires extremely high combustion temperatures to heat the reaction mixture to the operating temperature. Heating up the gases by combustion implies high CO_2 emissions, which should be reduced in order to reduce the environmental impact. On the other hand, the adoption of an heat medium completely decoupled from the reaction allows to find different path in order to make the whole process decarbonized or with low associated GHGs emissions.

2 | Bayonet-tube biogas reformer

In this chapter the bayonet-tube reformer studied in this thesis work will be presented. Initially an overview of the process will be given in order to clarify the key aspects that characterize the reformer. In the second section, the challenges related to the adoption of an heat exchange reformer will be highlighted, focusing on the particular geometry of the reactor. In the third and last section the introduction of baffles, their shape and characteristics will be considered, focusing on the reasons behind the necessity of introducing them.

2.1. Reformer characterization

The bayonet-tube reformer considered in this thesis work is thought for small scale applications, in which a synthesis gas suitable for synthetic fuels production, through a Fischer-Tropsch process, is obtained from a biogas feed. The biogas feed, coming from an anaerobic digestion unit, is mainly composed of CH_4 and CO_2 which makes it perfect for undergoing a Dry Reforming process. The Dry Reforming process is strongly endothermic and a large quantity of heat needs to be supplied in order to let the reactions proceed towards the desired products, which are CO and H_2. The peculiarity of this reformer is related to the heat source adopted. As underlined in chapter 1, in non-autothermal reforming process, the heat required for the steam or dry reforming reactions is made available by combustion, usually of a portion of the feed. This methodology introduces large CO_2 emissions in the environment. In the bayonet-tube biogas reformer analyzed here, the heat source is a solar tower, which receives water at atmospheric pressure and makes available to the reformer superheated steam at high temperature. It is of key importance to underline that this solution makes the whole process carbon-neutral, being the energy available from the solar tower completely renewable and considering that the life-cycle of the biomass accounts for a net-zero CO_2 emissions, considering that the carbon atoms present in the biomass have been produced by subtracting CO_2 from the environment. Returning on the reformer configuration, the presence of an heat transfer fluid makes this technology similar to the heat exchange reformers presented in the ded-

icated section. Other than the consequences of adopting a convective heat transfer in the reformer, aspect that will be deepened throughout all this work, it is important to underline that part of the superheated steam, generated by the solar tower, is mixed with the biogas feed. This choice brings multiple avdvantages. First of all, the process is no more Dry Reforming but Bi-reforming, which is less endothermic and allows to obtain a wider range of H_2/CO of syngas, by modifying the H_2O quantity in the feed. On the other hand, the presence of steam is beneficial for the life of the catalyst because reduces the tendency of coke formation, that is active in the operative range of the reactor and with the considered catalyst, which is Nickel (Ni).

2.2. Constructive design

The definition of heat exchange reformer is related to the presence of the heat transfer fluid, as a medium between the solar tower and the reactants side, which is different from the other technology in which the heat transfer is direct from the heat source to the reactants. The peculiarities of the bayonet-tube reformer analyzed in this thesis work make necessary to study a completely different design for the reformer itself. The complete geometry of the reformer unit is characterized by a shell with an optimized number of bayonet tubes inside it, but, due to the early stage of the project and the complex geometry of the complete reformer, difficult to be addressed in a CFD simulation and with prohibitive computational cost, a simplified geometry has been considered. As shown in figure 2.1, the simplified reformer is characterized by two main components, which are the shell and the bayonet-tube. Inside the shell, the superheated steam, produced by the solar tower, flows from the bottom to the top of the reactor. The flow of the reactants/products inside the bayonet-tube is more complex. The biogas feed, enriched with steam, enters through the annular section, present at the top of the tube. In the first part of the tube, characterized by an annular shape, the catalyst is present, in form of pellets, and the reforming reactions are carried out. In the bottom part of the bayonet-tube, the flow undergoes a strong deviation and is redirected, into the central part, towards the top of the bayonet-tube. It is important to underline that the reforming reactions occur only in the annular part and that the flow into the central part is already reacted and it is high temperature syngas. This feature is of key importance because clarifies the choice of this configuration. In particular the reformer introduces a counter-current flow configuration of the reacting flow (biogas) with both the superheated steam and the syngas produced. The counter-current disposition between the reactants and the heat transfer fluid is necessary in order to enhance the heat transfer between the two zones, allowing to recover the highest possible quantity of thermal power from the superheated steam. The

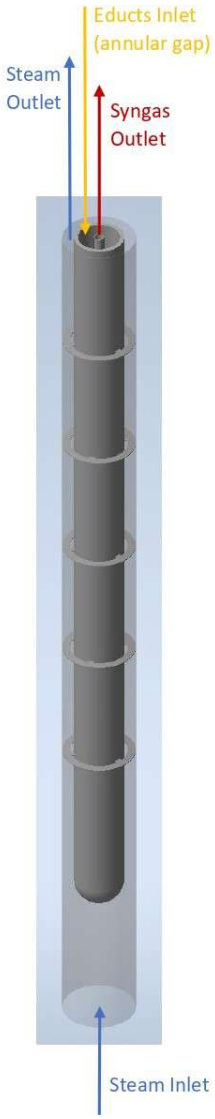

Figure 2.1: Bayonet tube-reformer layout

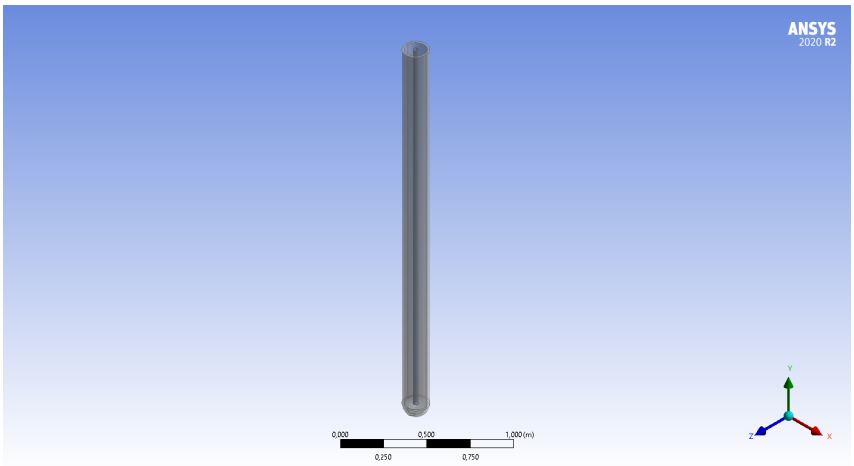

Figure 2.2: Bayonet tube reformer

introduction of baffles is headed towards this direction too. For which regards the adoption of the bayonet-tube configuration, this choice has been done in order to recover heat from the high temperature syngas that is already reacted, increasing the efficiency of the whole process, while producing syngas at lower temperature. Clearly increasing the heat transfer to the reactants side is beneficial for the correct proceeding of the reforming reactions. The reformer's bayonet shape introduces this advantage but shows some drawbacks too, mostly related to the strong deviation imposed to the flow in the bottom part of the reformer, increasing in this way the pressure drop in the biogas/syngas side. For which regards the heat transfer fluid side, most of the work has been performed by introducing spider baffles, in order to generate and enhance turbulence to reach high velocities and high heat transfer through convection, that is the predominant kind of heat transfer in this reformer. Heat transfer properties are of key importance in the analysis and optimization of the biogas reformer. In particular convective heat transfer between the heat transfer fluid and the biogas side needs to be maximized in order to reach high conversion of CH_4 and high concentration of H_2 and/or CO in the product to obtain high quality syngas, feasible to undergo further processes. Heat transfer between the heat transfer fluid and ambient has to be considered too, to make the problem as realistic as possible; in order to limit this thermal exchange between the two side an insulating layer is considered in the shell of the reactor. As already highlighted, convection is the most important aspect to be considered for the heat transfer, but radiation needs to be considered too, due to the high inlet temperatures of the superheated vapour. In a previous work, carried out on a geometry completely similar to the one shown in figure 2.1 but without the baffles, it has been noticed that the most of the heat exchanged between the heat transfer fluid side and the reactants side, was coming from radiation, while, in the plain configuration,

convective heat transfer was really poor. This consideration brought to the decision of introducing the baffles to enhance the convective heat transfer. In fact the superheated steam flow, in the plain configuration, is laminar and poor heat transfer properties are expected under this flow regime.

2.3. Spider baffles

The introduction of baffles and the effect generated by their geometrical shape is the key aspect of this thesis work. Baffles are solid components, like panels or vanes, that are used mostly in heat exchangers to promote turbulence and enhance the convective heat transfer, due to the increasing velocity of the flow where baffles are displaced; on the other hand, baffles are used to hold the tubes in position, because the flow, if characterized by an high velocity, could bend the tubes and eventually break them, considering that in most of the application where baffles are adopted, the flow is at high temperature too. Various baffles layout are available and different configurations and dispositions can be considered for different applications. In the reformer object of this thesis work, a particular kind of baffles, known as spider baffles, have been considered; in particular, five baffles, distributed at equal distance one from the other (Fig. 2.4), are introduced in the heat transfer fluid side, fixed to the internal part of the shell and hooked to the external part of the reformer outer tube through stands-off, in order to center the tube, as represented in figure 2.4 and 2.5.

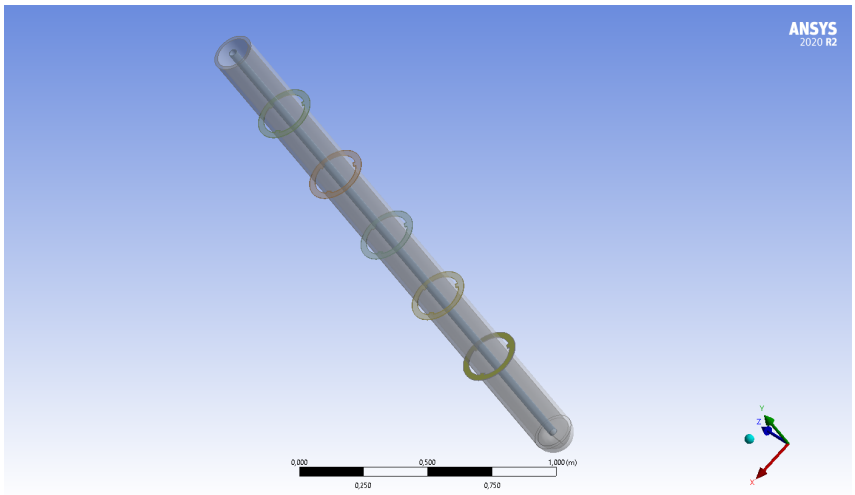

Figure 2.3: Reformer tube 5 baffles: side view

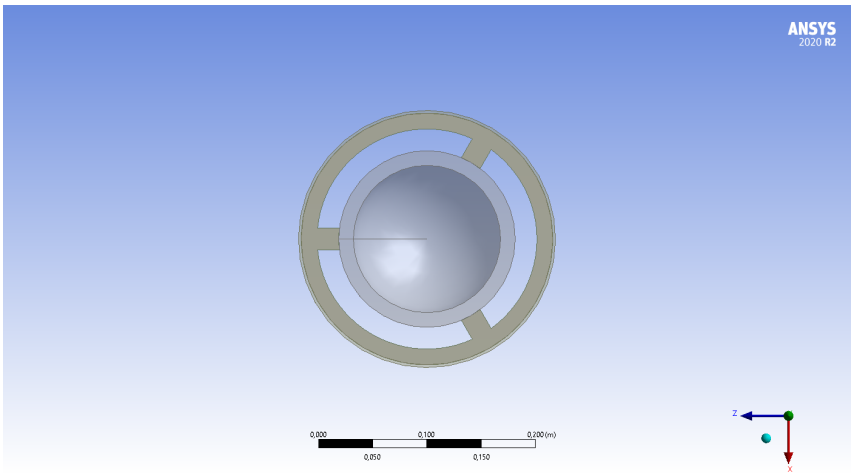

Figure 2.4: Spider baffle with 20 mm radial gap

This figure shows the first spider baffle, with a view from the top of the reformer, to better clarify the geometry studied, because it is of key importance. A feature to underline about this layout, is the radial gap present between the baffle and the reformer outer tube; in this zone the section available for the flow is strongly reduced, so that, following the continuity equation, the velocity of the flow will strongly increase while passing through the gap creating vortexes downstream the baffle. This effect is crucial to enhance turbulence and convective heat transfer in the superheated steam side. The radial gap is a geometrical parameter that can be modified and, in this thesis work, baffles with 20 mm and 10 mm radial gap have been considered.

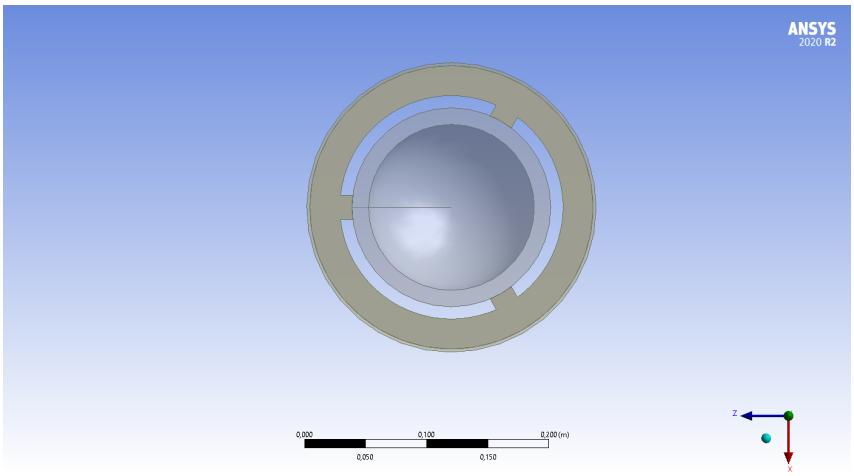

Figure 2.5: Spider baffle with 10 mm radial gap

As it can be clearly seen, the section available for the flow is strongly reduced from the configuration with 20 mm of radial gap to the configuration with 10 mm of radial gap,

which will be beneficial in terms of heat transfer properties, because the lower the section, the higher the velocity, the higher the heat transfer coefficient, roughly, but detrimental in terms of pressure drops due to the strong deviations imposed to the flow, that without baffles would be mostly axial. The last thing that needs to be underlined is that all the baffles are displaced in the same way. In other terms, the baffles are not rotated one with respect to the other, and this lead to have a symmetrical geometry every 120°.

3 | CFD modelling: theoretical background

In this chapter a review of all the models adopted to carry out the CFD simulations on the reactor will be highlighted in order to show and explain the theory and equations behind the different models selected.

3.1. Mesh

Meshing is a key step while approaching a CFD problem. A good mesh is fundamental in order to reach good and accurate results and a low quality mesh can lead to convergence issues while simulating. For this reason it is important to underline what is the mesh, its main characteristics and what are the aspects to take into account while creating a mesh. The mesh is the discretization of a continuum domain into discrete volumes of different dimensions, the cells. This process is done with the aim of dividing the continuum in a discretized volume made of an high number of cells, in order to evaluate the variables of the problem by solving the equations representing the physics of the process, in the cell centre. While creating a mesh, some requirements need to be met; high density of cells is required where steep gradients are expected or where the geometry shows fine details, whereas in zone in which there are no strong deviations, a coarse mesh is preferable. On the other hand solution accuracy and stability depends on the shape of mesh cells and on how the cells are displaced in the volume. A key aspect to take into account is related to the computational effort required while simulating a CFD problem, which is strongly dependent on the mesh, mainly on the number of cells, but even on the type of cells. This thesis work has been carried out on a 3D geometry and so a 3D mesh has been created. There are various possible three dimensional mesh elements: thetrahedal, pyramidal, prismatic, hexahedral or polyhedral. In general a mesh can be of three different types: structured, unstructured or multi-block. A structured grid has a lower cell count with respect to an unstructured one for the same geometry but it is possible to have a structured mesh only for geometrically simple domains. An unstructured mesh is required

while approaching complex 3D problems; this kind of mesh has the drawback of an higher cell count with respect to a structured one but with the advantage of giving the possibility of using cells of different kind, depending on the geometrical shape of the region that needs to be fitted. Both these two types of mesh are composed by a single block of cells, while a multi-block mesh, as the name suggests, is composed by more than one block and the different blocks can be structured or unstructured. In order to evaluate the quality of a mesh, a set of quality metrics are considered, such as skewness, orthogonal quality and aspect ratio. Skewness evaluates, for a single cell, a normalized angle deviation, considering this formulation:

$$S_k = \max[\frac{\theta_{max} - \theta_e}{180 - \theta_e}, \frac{\theta_e - \theta_{min}}{\theta_e}] \tag{3.1}$$

The optimal value for skewness is zero and in general needs to be as low as possible. Orthogonal quality considers the disposition of the faces in space, by evaluating two parameters as shown here:

$$O_{q,1} = \frac{\boldsymbol{A}_i \cdot \boldsymbol{f}_i}{|\boldsymbol{A}_i| \cdot |\boldsymbol{f}_i|} \tag{3.2}$$

$$O_{q,1} = \frac{\boldsymbol{A}_i \cdot \boldsymbol{c}_i}{|\boldsymbol{A}_i| \cdot |\boldsymbol{c}_i|} \tag{3.3}$$

where A_i is the vector normal to the i^{th} face, f_i is a vector from the centre of the cell to the centre of the i^{th} face and c_i is the vector connecting the centre of the i^{th} cell with the centre of the adjacent cell that shares the same face. These two values are computed for each face, then the minimum value obtained is the orthogonal quality of the cell. The orthogonal quality of each cell needs to stay over 0.75 and in general as close as possible to unity. The aspect ratio considers quantity of a single cell, as orthogonal quality and skewness, and evaluates an adimensional value that is used to understand the difference between the cell dimension; it can be computed in various way depending on the software. One last important feature to consider is that is crucial to avoid strong local deviations, in terms of cells dimensions, from cells to cells. All these parameters can be evaluated once the mesh is done, but it is possible that even using a good quality mesh, the solution is dependent on the mesh, which means that, the same problem, with a different mesh, gives different results. In order to avoid this problem, performing a mesh independence study, consisting in simulating the problem with different mesh, ensuring that the results are similar, is of key importance.

3.2. Solver theory and governing equations

The volume discretization process, described in the last section, is fundamental because it allows ANSYS Fluent to discretize and linearize the governing equations for the discrete dependent variables, in order to solve them in every control volume, which are the single cells, of the mesh. In ANSYS Fluent two solvers are available [51]: the pressure-based solver and the density-based solver. Historically speaking, the pressure-based solver was introduced to approach low-speed incompressible flows while the density-based solver was developed to address high-speed compressible flows. The two methods have been updated throughout the years and now are able to solve a wide range of problems, beyond their original intent. The difference between the two methods can be found in the different approach used to linearize and solve the problem. The pressure-based solver has been used in this thesis work, due to the nature of the problem, and, in this section, there will be a focus on this numerical method. However, it is essential to understand first how ANSYS linearizes differential equations, focusing on how the known variables at the center of the cells are used to interpolate the variables present, for example, on the cell face.

3.2.1. General scalar transport equation discretization

ANSYS Fluent employs a control-volume-based method that transforms a scalar transport equation into an algebraic equation that can be solved numerically. This technique involves integrating the transport equation for each control volume to create a discrete equation that expresses the conservation law applied on the control volume. To understand the discretization of the governing equations, it is possible to consider the unsteady transport equation for a generic scalar quantity ϕ. The integration of the equation considered on a generic control volume V can be expressed as follows:

$$\int_V \frac{\partial \rho\phi}{\partial t} dV + \oint \rho\phi \boldsymbol{U} \cdot d\boldsymbol{A} = \oint D_\phi \nabla\phi \cdot d\boldsymbol{A} + \int_V S_\phi dV \tag{3.4}$$

This kind of equation is applied in every control volume present in the mesh, so in every cell in other terms, clearly representing different dependent variables of the flow. Before starting the solution process, the equation 3.4 has to be discretized as follows:

$$\frac{\partial \rho\phi}{\partial t} V + \sum_{f=1}^{N_{faces}} \rho_f \boldsymbol{U}_f \phi_f \cdot \boldsymbol{A} = \sum_{f=1}^{N_{faces}} D_\phi \nabla\phi_f \cdot \boldsymbol{A}_f + S_\phi V \tag{3.5}$$

where all the terms with the subscript f are evaluated at the face of the cell. The equations that ANSYS Fluent solves have a similar structure to the one described above. The scalar transport equation in a discretized form (eq. 3.5), involves the scalar variable ϕ that is unknown at the center of the cell, along with the unknown values in the neighboring cells. Typically, this equation is nonlinear with regards to these variables. However, it is possible to formulate a linearized version of the equation, as follows:

$$a_p \phi = \sum_{nb} a_{nb} \phi_{nb} + b \tag{3.6}$$

where the subscript nb refers to neighbour cells a_p and a_{nb} are the linearized coefficients for ϕ and ϕ_{nb} respectively. Equations of a similar form can be written for every cell in the mesh, which gives rise to a set of algebraic equations characterized by a sparse coefficient matrix. By solving these equations, it is possible to compute all the considered dependent variables at the centre of every cell, for example for every cell a single value of pressure, temperature, x-component of the velocity and in general a generic scalar variable ϕ, will be computed. On the other hand, as it is possible to notice in equation 3.5, discrete values of the scalar variables at the faces of the cells are needed to solve the transport equations, in the convective and diffusive terms, so a method to evaluate this scalar quantities is adopted.

3.2.2. Scalar variables discrete profile interpolation

The interpolation of the scalar variables is fundamental to resolve the transport equations in every cell of the mesh. In particular both a spacial and a temporal interpolation is needed when an unsteady problem is being simulated. Considering only a spacial problem, as already specified, ANSYS Fluent typically stores scalar values discretely at the cell centers, but for the convection terms in Equation 3.5, face values are required, and must be obtained by interpolating from the cell center values using an upwind scheme. The upwind scheme derives the face value from the quantities in the cell that is "upwind" relative to the direction of the normal velocity. Various upwind schemes are available in ANSYS fluent but in this brief section only two will be highlighted. The first one is the first-order upwind scheme, in which the values of the quantities at cell faces are determined by assuming that the cell-center values of any field variable represent a cell-average value that holds true throughout the cell. This means that the face quantities are identical to the cell quantities. Therefore, when first-order upwinding is selected, the face value ϕ_f is set to be equal to the cell-center value ϕ in the upstream cell. The other scheme considered here is the second-order upwind scheme, in which to compute the quantities at

cell faces, a multidimensional linear reconstruction approach is employed. This approach utilizes a Taylor series expansion of the cell-centered solution about the cell centroid to achieve higher-order accuracy at cell faces. Therefore, when second-order upwinding is selected, the face value is calculated using the following expression:

$$\phi_f = \phi + \nabla\phi \cdot \boldsymbol{r} \tag{3.7}$$

where $\nabla\phi$ is the gradient of the scalar quantity considered, in the upstream cell, and $\boldsymbol{r}$ is the spatial vector from the upstream cell centroid to the face centroid. The temporal discretization is not addressed here because the problem studied in this thesis work is stationary. On the other hand, some method to evaluate the gradient of the variables needs to be introduced. The construction of scalar values at cell faces, as well as the computation of secondary diffusion terms and velocity derivatives, both require gradients. The gradient of a specific variable is utilized to discretize the convection and diffusion terms in the equations of flow conservation. The method used in this thesis work, to evaluate gradients is called least squares cell-based. The key assumption of this method is that the variation of the generic scalar variable, ϕ, is linear from cell to cell, so that it is possible to evaluate the change in cell values between two different cells, c_0 and c_1, along the vector δr_i connecting the centroid of the two cells, using this formulation:

$$(\nabla\phi)_{c_0} \cdot \Delta r_i = (\phi_{c_i} - \phi_{c_0}) \tag{3.8}$$

By writing this equation for every cell surrounding the considered one, the following system is obtained:

$$[J](\nabla\phi)_{c_0} = \Delta\phi \tag{3.9}$$

where $[J]$ is the coefficient matrix, completely defined by the geometry. By solving this system is possible to obtain the gradient of the considered scalar variable:

$$\nabla\phi_0 = \phi_x \boldsymbol{i} + \phi_y \boldsymbol{j} + \phi_z \boldsymbol{k}$$

3.2.3. Pressure-based solver

The pressure-based solver uses a projection method algorithm. This method ensures that the constraint of mass conservation for the velocity field is met by solving a pressure equation. The pressure equation is obtained from the momentum and continuity equations in such a way that the corrected velocity field satisfies the continuity. Since the governing equations are nonlinear and interdependent, the solution process involves iterations where

the entire set of governing equations is repeatedly solved until the solution converges. In ANSYS Fluent two different pressure-based solver algorithms are available and, even if only one has been adopted in this thesis work, both of them will be highlighted here to better explain the working process. The first algorithm is the pressure-based segregated algorithm. This method is called segregated because the governing equations of the flow are solved, for the dependent variables of the problem, sequentially, or, in other words, one after another. Hence the different equations are decoupled or segregated. This solver is memory efficient, because only one equation is solved at a time. On the other hand, the drawback of this algorithm is a slow convergence of the solution, related to the sequential approach to the single equations. Here follows the steps of the segregated algorithm:

1. Update the fluid properties based on the current solution.
2. Solve the momentum equations, in a sequential way, considering the values of pressure and face mass flux computed in the last iteration.
3. Solve the pressure correction equation using the velocity field and mass flux updated by the solution of the momentum equations.
4. Update all the flow variables (face mass flux, pressure and velocity field) using the values obtained in step 3.
5. Solve the equations for the other dependent variables, such as turbulence, energy and radiation intensity.
6. Compute the residuals between the updated variables and the one from the old iteration.

The other pressure-based solver algorithm present in ANSYS Fluent is the coupled algorithm. The pressure-based coupled algorithm differs from the segregated algorithm mentioned earlier because it solves a system of coupled equations that includes the momentum equations and the pressure-based continuity equation. As a result, in the coupled algorithm, steps 2 and 3 of the segregated solution algorithm are replaced by a single step in which the coupled system of equations is solved. The remaining equations are solved independently, similar to the segregated algorithm. Due to the coupled manner in which the momentum and continuity equations are solved, the rate of solution convergence is significantly better than that of the segregated algorithm. However, the memory requirement increases by 1.5 to 2 times that of the segregated algorithm because the discrete system of all momentum and pressure-based continuity equations must be stored in memory when solving for the velocity and pressure fields (as opposed to just a single equation, as in the case of the segregated algorithm). It is important to focus now on the effective

way in which the pressure-based solver solves the momentum and continuity equations. First of all, the two equations are discretized, considering the integral on a control volume, the single cell, as follows:

$$\oint \rho \boldsymbol{U} \cdot d\boldsymbol{A} = 0 \tag{3.10}$$

$$\oint \rho \boldsymbol{U}\boldsymbol{U} \cdot \boldsymbol{A} = -\oint pI \cdot d\boldsymbol{A} + \oint \overline{\overline{\tau}} \cdot \boldsymbol{A} + \int_V \boldsymbol{F} dV \tag{3.11}$$

where the first is the continuity equation and the second is the momentum equation. For which regards the discretization and linearization of the momentum equation, eq. 3.11, it is possible to consider the same discretization scheme already described for the general scalar equation. For example the x-momentum equation can be expressed as follows:

$$a_p U_x = \sum_{nb} a_{nb} U_{x,nb} + \sum p_f A \cdot \boldsymbol{i} + S \tag{3.12}$$

If the pressure field and face mass fluxes are known, the equation 3.12 can be solved using the method outlined earlier in this section to obtain a velocity field. However, since the pressure field and face mass fluxes are not initially known, they must be obtained as part of the solution. Addressing important issues related to the storage of pressure and the discretization of the pressure gradient term is crucial in this process. ANSYS Fluent adopts a co-located scheme where pressure and velocity are stored at the center of the cells. However, when using Equation 3.12, the pressure value at the face of the cell is required, which necessitates an interpolation scheme to calculate the pressure face values from the cell values. The pressure interpolation scheme considered here is called Second Order scheme, which is the default one in ANSYS Fluent and has the following formulation:

$$P_f = \frac{1}{2}(P_{c_0} + P_{c_1}) + \frac{1}{2}(\nabla P_{c_0} \cdot \boldsymbol{r_{c_0}} + \nabla P_{c_1} \cdot \boldsymbol{r_{c_1}}) \tag{3.13}$$

where c_0 and c_1 are the two cells that share the face f where the pressure value is being computed. Regarding the discretization of the continuity equation, it is possible to express it with the following formulation:

$$\sum_{f}^{N_{faces}} J_f A_f = 0 \tag{3.14}$$

where J_f is the mass flux through face f, defined as:

$$J_f = \rho U_n \tag{3.15}$$

As previously noted, the pressure-based solver in Ansys Fluent allows to solve flow problems using either a segregated or a coupled approach. The coupled scheme has several advantages over the non-coupled or segregated approach, as it provides a robust and efficient single-phase implementation for steady-state flows, resulting in superior performance compared to segregated solution schemes. The coupled algorithm solves the momentum and pressure-based continuity equations simultaneously. This is achieved by using an implicit discretization of the pressure gradient terms in the momentum equations and the face mass flux in the continuity equations, which results in a fully implicit coupling between the equations.

3.3. Heat transfer

Correctly modelling heat transfer is crucial to obtain solid results in mostly every engineering application where two fluids are exchanging high quantities of thermal power. Usually, there are three primary ways in which heat can be transferred: conduction, convection, and radiation. While the physical models used for conduction and convection are relatively straightforward, more intricate models are needed to account for radiation. As a result, the initial portion of the section will deal with the standard heat transfer equation, and the second portion will concentrate on radiative heat transfer.

3.3.1. Conduction and convection

The standard equation that ANSYS Fluent solves while addressing heat transfer is expressed as follows:

$$\frac{\partial}{\partial t}(\rho(e+\frac{U^2}{2})+\nabla\cdot(\rho\boldsymbol{U}(h+\frac{U^2}{2}))=\nabla\cdot(k\nabla T-\sum_j h_j\boldsymbol{J}_j+\overline{\tau}_{eff}\cdot\boldsymbol{U})+S_h \tag{3.16}$$

The equation comprises of five terms, with the first term representing the unsteady term that pertains to accumulation. The second term relates to convection, while the three terms on the right-hand side signify conduction, species diffusion, and viscous dissipation, respectively. Additionally, the term S_h denotes volumetric heat sources that are defined by the user and the heat generation rate from chemical reactions, which will be elaborated on later. In the above equation, enthalpy, for ideal gas as follows:

$$h=\sum_j Y_j h_j \tag{3.17}$$

and for incompressible materials includes the pressure contribution:

$$h = \sum_j Y_j h_j + \frac{p}{\rho} \tag{3.18}$$

where in both formulations, h_j is defined as:

$$h_j = \int_{T_{ref}}^{T} c_{p,j} dT \tag{3.19}$$

where T_{ref} is equal to $298.15K$, the default value when the pressure-based solver is adopted. Equation 3.10 incorporates pressure work and kinetic energy terms, which are usually insignificant in incompressible flows. Consequently, the pressure-based solver, by default, excludes the pressure work and kinetic energy terms when solving for incompressible flow. The term S_h in the heat transfer equation accounts for source of energy and in particular accounts for the energy source from chemical reactions, as follows:

$$S_h = -\sum_j \frac{h_j^0}{M_j} R_j \tag{3.20}$$

where h_j^0 is the enthalpy of formation of species and R_j is the volumetric rate of creation of species, as it will be explained in the dedicated section of this chapter. In solid regions, the energy transport equation used by ANSYS Fluent as the following formulation:

$$\frac{\partial}{\partial t}(\rho h) + \nabla \cdot (\boldsymbol{U} \rho h) = \nabla \cdot (k \nabla T) + S_h \tag{3.21}$$

where there are the same global terms of equation 3.10, but for stationary walls the convective term is zero.

3.3.2. Radiation

Radiation is not considered in the general energy transport equation and here the problem will be addressed singularly. Radiation is important to be considered when the radiant heat flux

$$Q_{rad} = \sigma (T_{max}^4 - T_{min}^4) \tag{3.22}$$

is large compared to the heat transfer rate due to convection or conduction. This usually happens at high temperatures because the radiative heat flux has a fourth-order dependence on temperature, indicating that radiation becomes the dominant form of heat transfer. Radiation travels in straight lines, that are beam directions, and it is defined by

its intensity, I, which is a function of its coordinates in space $\boldsymbol{r} = (x, y, z)$ and, differently from all the other variables, it is a function of its direction too, $\boldsymbol{s} = (s_x, s_y, s_z)$. This is a major aspect to be noticed because it makes the solution of the radiative problem a lot more complex. In order to correctly address radiation, radiative transport equation (RTE) needs to be solved:

$$\frac{dI(\boldsymbol{r}\boldsymbol{s})}{ds} + (a + \sigma_s)I(\boldsymbol{r}, \boldsymbol{s}) = an^2\frac{\sigma T^4}{\pi} + \frac{\sigma_s}{4\pi}\int_0^{4\pi} I(\boldsymbol{r}, \boldsymbol{s'})\Phi(\boldsymbol{s}, \boldsymbol{s'})d\Omega' \tag{3.23}$$

where $\boldsymbol{s'}$ is the scattering direction vector. As already underlined, going through the equation it is clear that the only link between radiation and the flow properties is the temperature and this particular will be useful when considering how often is necessary to solve radiation equation during the simulation. Considering now the complete equation it is possible to see that is composed by four different terms: rate of change, absorption, emission and scattering terms. The rate of change accounts for the variation in intensity in the same direction in the space coordinates. Absorption is a negative source term and accounts for the radiation absorbed by the bodies, reducing the beam intensity while emission is a positive source term, related to the radiation emitted by the bodies and it is proportional to T^4. The scattering term is the most complex one, in fact allows to account for transfer energy between the different beam directions, in term of radiation intensity. In other words it accounts for the energy transferred to a certain beam direction from all the other possible directions and so acts as a source. This term is mathematically described by an integral on a circumference and clearly in CFD simulations all the possible beam directions need to be discretised in a finite number of possible directions. Considering that radiation travels in a straight line, that is the beam direction, from a point, in 3D, all the perpendicular lines to the surface of a sphere are the possible infinite directions. The discrete ordinates (DO) radiation model resolves the radiative transfer equation (RTE) by using a finite number of discrete solid angles. Each solid angle is connected with a vector direction $\boldsymbol{s}$, which remains fixed in the global Cartesian system. The DO model considers the radiative transfer equation in the direction $\boldsymbol{s}$ as a field equation, which is rewritten as follows:

$$\nabla \cdot (I(\boldsymbol{r}, \boldsymbol{s})\boldsymbol{s}) + (a + \sigma_s)I(\boldsymbol{r}, \boldsymbol{s}) = an^2\frac{\sigma T^4}{\pi} + \frac{\sigma_s}{4\pi}\int_0^{4\pi} I(\boldsymbol{r}, \boldsymbol{s'})\Phi(\boldsymbol{s}, \boldsymbol{s'})d\Omega' \tag{3.24}$$

The angular space 4π at any given spatial location is divided into 8 octants, with each octant further subdivided into $N_\theta \cdot N_\phi$ control angles of extent ω_i. The polar and azimuthal angles, theta and phi respectively, are measured with respect to the global Cartesian system. The control angle's θ and ϕ extents, delta theta and delta phi, remain constant. In

two-dimensional calculations, only 4 octants are considered due to symmetry, resulting in a total of $4N_\theta N_\phi$ directions. In three-dimensional calculations, a total of $8N_\theta N_\phi$ directions are considered. For non-gray 3D models, $8N_\theta N_\phi$ equations are solved for each band. In the case of generalized unstructured meshes, the alignment of control volume faces with the global angular discretization is not guaranteed.

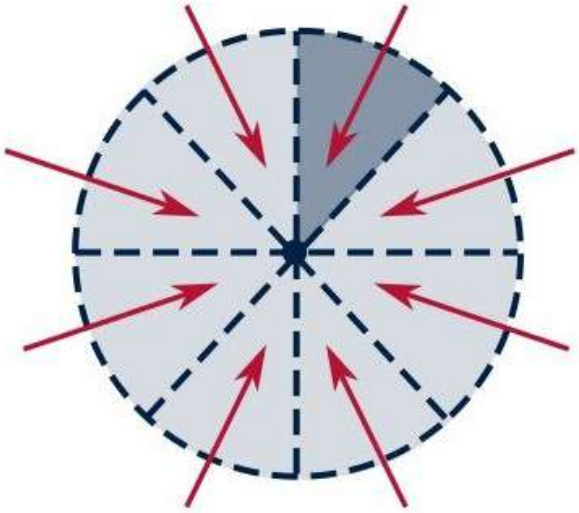

Figure 3.1: Octants discretization

3.4. Turbulence

Modelling turbulence correctly is fundamental in this CFD analysis because the aim of this work is to evaluate how the introduction of baffles, with different geometrical features, is effective in increasing the heat transfer between the two fluids. The relation between the presence of baffles and the increase in exchanged thermal power in the reactor can be found in the turbulence that is generated and enhanced in the heat transfer fluid zone by the baffles, because roughly, the higher the turbulence, the higher will be the convective heat transfer in the superheated vapour side. As already underlined, convection needs to be maximized in order to correctly feed the endothermic reactions occurring in the reactor side, so a precise evaluation of turbulence in the superheated vapour flow is of key importance. In CFD simulations, in particular in ANSYS fluent, it is possible to choose different models for turbulence, for example k-ϵ or k-ω, but before going through these models, that have been used in this work, it is important to clarify the role that these models play in solving the turbulence problem. Turbulent flows are approached by solving

the Reynolds-averaged Navier-Stokes equations, defined as follows:

$$\frac{\partial(\rho U_i)}{\partial t} + \frac{\partial}{\partial x_j}(\rho U_i U_j) = -\frac{\partial p}{\partial x_j} + \frac{\partial}{\partial x_j}[\mu(\frac{\partial U_i}{\partial x_j} + \frac{\partial U_j}{\partial x_i}) - \rho\overline{u_i' u_j'}] \tag{3.25}$$

In order to close this equation it is necessary to find a method to express the term:

$$\rho\overline{u_i' u_j'}$$

which is the Reynolds stress term, where u_i' and u_j' are the fluctuating components of the velocity. These fluctuating terms are averaged and needs to be express in terms of mean flow quantities; this is the turbulence closure problem. Eddy viscosity models, such as the k-ϵ and k-ω, are a class of turbulence models that allows to compute the Reynolds stress term. In order to express the Reynolds stress terms, the Boussinesq hypothesis needs to be introduced:

$$-\rho\overline{u_i' u_j'} = \mu_t \frac{\partial U}{\partial y} \tag{3.26}$$

in which μ_t is an artificial term, called turbulent viscosity, that gives the proportionality between the velocity gradient and the stress term. This equation is obtained and valid for a 1D flow moving in the x-direction and needs to be reformulated for a 3D problem. The full demonstration about how to move from the 1D formulation to the 3D one will be avoided, to not make this section too heavy, and only the final result will be considered. The 3D formulation of the Boussinesq hypothesis is expressed as follows:

$$-\rho\overline{u_i' u_j'} = \mu_t(\frac{\partial U_i}{\partial x_j} + \frac{\partial U_j}{\partial x_i}) - \frac{2}{3}\rho k \delta_{ij} \tag{3.27}$$

in which δ_{ij} is the Kronecker's delta. This equation can be used to evaluate the Reynolds stress term as a function of $\boldsymbol{U}(U_x, U_y, U_z)$ that is the mean flow velocity profile. The only thing missing to close the turbulence problem is to find a way to evaluate the turbulent viscosity μ_t; $k-\epsilon$ and $k-\omega$ models allow to compute the turbulent viscosity term in different ways. For this reason it is crucial to explain how these models work in order to notice the difference between the two.

3.4.1. k-epsilon turbulence models

Two-equation turbulence models, such as the standard $k-\epsilon$ model, determine both the turbulent length and time scales by solving two separate transport equations. Since its introduction by Launder and Spalding in 1971 [52][53][54], this model has become the most common choice for practical engineering flow calculations due to its robustness,

cost-effectiveness, and reasonable accuracy across a wide range of turbulent flows.

Standard k-epsilon turbulence model

The standard model is a modeling approach that employs transport equations to describe the behavior of turbulence kinetic energy and its dissipation rate. The turbulent dissipation rate ϵ is the rate characterizing the conversion of turbulent kinetic energy into thermal energy by viscosity and is defined as follows:

$$\epsilon = \nu \overline{\frac{\partial u_i' \partial u_j'}{\partial x_j \partial x_i}} \tag{3.28}$$

The standard model assumes that the flow is fully turbulent, and the impact of molecular viscosity is negligible. As a result, the standard model is only valid for fully turbulent flows. The transport equation for k is derived from the exact equation, while the transport equation for ϵ is obtained based on physical reasoning and differs significantly from its mathematically exact counterpart. The transport equations for the kinetic energy k and for the turbulent dissipation rate are expressed as follows:

$$\frac{\partial(\rho k)}{\partial t} + \nabla \cdot (\rho \boldsymbol{U} k) = \nabla \cdot [(\mu + \frac{\mu_t}{\sigma_k})\nabla k] + G_k + G_b - \rho\epsilon - Y_M + S_k \tag{3.29}$$

and

$$\frac{\partial(\rho \epsilon)}{\partial t} + \nabla \cdot (\rho \boldsymbol{U} \epsilon) = \nabla \cdot [(\mu + \frac{\mu_t}{\sigma_\epsilon})\nabla \epsilon] + C_1 \frac{\epsilon}{k}(G_k + C_3 G_b) - C_2 \rho \frac{\epsilon^2}{k} + S_\epsilon \tag{3.30}$$

In these equations, G_k refers to the production of turbulence kinetic energy resulting from mean velocity gradients, while G_b represents the production of turbulence kinetic energy caused by buoyancy. Y_m denotes the contribution of fluctuating dilatation in compressible turbulence to the total dissipation rate. The constants C_1, C_2, and C_3 have fixed values. The turbulent Prandtl numbers for k and ϵ are represented by σ_k and σ_ϵ, respectively. Lastly, S_k and S_ϵ are source terms that can be defined by the user. In this model, the turbulent viscosity, μ_t is computed as:

$$\mu_t = \rho C_\mu \frac{k^2}{\epsilon} \tag{3.31}$$

where C_μ is a constant value.

Realizable k-epsilon turbulence model

The Realizable $k-\epsilon$ model has demonstrated significant advancements over the standard $k-\epsilon$ model in scenarios where the flow displays pronounced streamline curvature, vortices, and rotation. Preliminary investigations have revealed that the Realizable $k-\epsilon$ model delivers superior performance compared to other $k-\epsilon$ model versions when validating flows that are separated or have complex secondary flow features. One of the primary drawbacks of traditional $k-\epsilon$ models is the modeled equation for the dissipation rate. The realizable $k-\epsilon$ model, proposed by Shih et al. [55] was intended to address these deficiencies of the standard $k-\epsilon$ model by introducing the following adjustments:

- A different eddy-viscosity formulation that involves a variable C_{mu}
- A new model equation for the turbulent dissipation rate, ϵ, based on the mean-square vorticity fluctuation

Here follows the transport equations for k and ϵ:

$$\frac{\partial(\rho k)}{\partial t} + \nabla \cdot (\rho \boldsymbol{U} k) = \nabla \cdot [(\mu + \frac{\mu_t}{\sigma_k})\nabla k] + G_k + G_b - \rho\epsilon - Y_M + S_k \tag{3.32}$$

and

$$\frac{\partial(\rho \epsilon)}{\partial t} + \nabla \cdot (\rho \boldsymbol{U} \epsilon) = \nabla \cdot [(\mu + \frac{\mu_t}{\sigma_\epsilon})\nabla \epsilon] + \rho C_1 S\epsilon - \rho C_2 \frac{\epsilon^2}{k + \sqrt{\nu\epsilon}} + C_{1\epsilon}\frac{\epsilon}{k} C_{3\epsilon} G_b + S_\epsilon \tag{3.33}$$

where:

- $C_1 = max[0.43, \frac{\eta}{\eta+5}]$
- $\eta = S\frac{k}{\epsilon}$
- $S = \sqrt{2 S_{ij} S_{ij}}$
- $S_{ij} = \frac{1}{2}(\frac{\partial U_j}{\partial x_i} + \frac{\partial U_i}{\partial x_j}$

It is possible to notice that the transport equation for k is the same of the standard $k-\epsilon$ model, except for the values of the constants, whereas the transport equation for ϵ is quite different. The turbulent viscosity is computed from its definition:

$$\mu_t = \rho C_\mu \frac{k^2}{\epsilon} \tag{3.34}$$

with the important aspect being the fact that C_μ is not considered as a constant, but it is computed as follows:

$$C_\mu = \frac{1}{A_0 + A_s \frac{kU^*}{\epsilon}} \tag{3.35}$$

where the term U^* is a function of the mean strain and rotation rates of the flow. The model constants have been established to ensure that the model performs well for certain canonical flows:

- $C_{1\epsilon}$=1.44
- C_2=1.9
- $\sigma_k = 1$
- $\sigma_\epsilon = 1.2$

3.4.2. k-omega turbulence models

The $k-\epsilon$ turbulent model has some limitations, related for example to the accuracy in predicting boundary layers with adverse pressure gradients or supersonic flows with shock waves presence. For this reason many different models have been proposed. The most popular model to address this kind of situation is the $k-\omega$ model, initially introduced in 1988 by Wilcox. This model relies on ω instead of ϵ, where ω is the specific turbulence dissipation rate, defined as follows:

$$\omega = \frac{\epsilon}{C_\mu k} \tag{3.36}$$

being C_μ a constant coefficient but ϵ, as already shown, cannot be computed directly being a function of fluctuating variables of the flow. According to this, a transport equation needs to be solved to compute ω. The transport equation for ω is as follows:

$$\frac{\partial(\rho\omega)}{\partial t} + \nabla \cdot (\rho \boldsymbol{U} \omega) = \nabla \cdot ((\mu + \frac{\mu_t}{\sigma_k})\nabla\omega) + \frac{\gamma}{\nu_t} P_k - \beta\rho\omega^2 \tag{3.37}$$

Theoretically it is possible to compute ϵ from ω and viceversa so the two models are really similar. The main difference is that, while the $k-\epsilon$ model needs dumping functions in the viscous sub-layer, which are not too accurate, the $k-\omega$ model does not need any dumping function and it is more accurate while approaching the viscous sub-layer. The standard $k-\omega$ model has a major drawback because is strongly dependent on the freestream values of k, ϵ and ω, which is resulting in non accurate solution while non addressing the viscous sub-layer. In order to solve this issue another model has been presented, the $k-\omega$ SST model, which adopts the $k-\omega$ model near the wall, where viscous effects are

important (Re_T is small), the k-ϵ model far from the wall, where inertial effects are more important (Re_T is large) and for the intermediate condition, a blend between the two models is adopted. In order to understand how this particular model works it is necessary to rearrange some equations. In particular, it is possible to rewrite the transport equation for ϵ, as shown in the $k-\epsilon$ model section, by substituting ϵ using the definition of ω:

$$\epsilon = C_\mu k\omega \tag{3.38}$$

obtaining the following equation in ω:

$$\frac{\partial(\rho\omega)}{\partial t} + \nabla\cdot(\rho\boldsymbol{U}\omega) = \nabla\cdot((\mu + \frac{\mu_t}{\sigma_k})\nabla\omega) + \frac{\gamma}{\nu_t}P_k - \beta\rho\omega^2 + 2\frac{\rho\sigma_\omega}{\omega}\nabla k : \nabla\omega \tag{3.39}$$

By comparing this equation with equation 2.13, transport equation for ω, it is possible to notice that they differ only for the last term, which is missing from the previous equation. Multiplying this term by (1-F_1) it is possible to switch from $k-\epsilon$ to $k-\omega$ model. In particular when $F_1 = 1$, the additional term vanish and the equation represents the transport equation for ω and so $k-\omega$ model, while if $F_1 = 0$, the equation is the transport equation for ϵ and represents the $k-\epsilon$ model; by adopting values between 0 and 1 it is possible to blend the two different models. Usually high values are used near the wall, where $k-\omega$ model is more accurate than $k-\epsilon$, and low values far from the wall where it is better to adopt $k-\epsilon$ model.

3.4.3. Wall functions

Turbulent flows are significantly affected by the presence of the wall and in this zone eddies and vortexes are often created. Other than this, due to the no-slip condition, steep gradients of velocity are present, and in general gradients of temperature and pressure are generated. For this reason is of key importance to model accurately the physics of the flow near to the walls. Considering that in a CFD mesh all the variables are evaluated at the centroid of every cell, the gradient between the variables are considered linear between one cell to another; this could be a problem near to the wall where the gradients of the variables are large. In order to solve this problem should be necessary to have a really fine resolution of the mesh near to the walls to evaluate accurately the behaviour of the variables' profile. On the other hand, too thin cells result mostly in poor cell quality, high aspect ratios and a too high number of cells that can decrease the convergence velocity and stability quite significantly. For this reason, wall functions are used in CFD applications in order to approximate correctly the flow variables' behaviour

near the wall reaching accurate results, without having too thin cells in the mesh, avoiding the drawbacks highlighted above. Wall functions are empirical functions, fitted on the real behaviour of the flow near to the wall and are used in every CFD simulation.

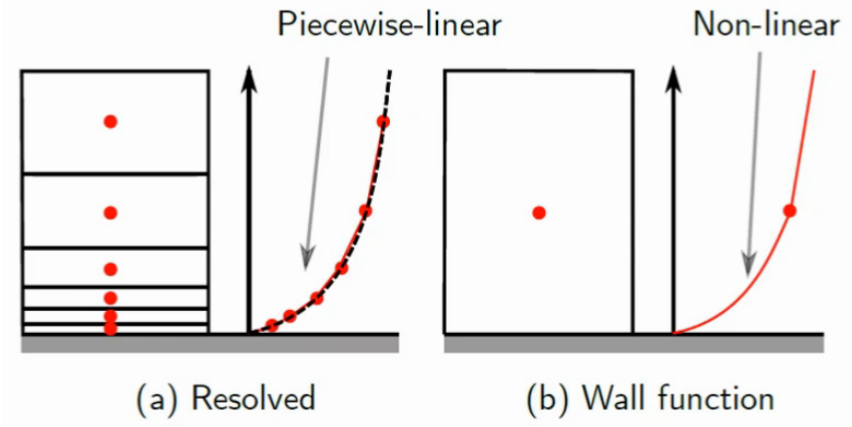

Figure 3.2: Resolved mesh vs Wall functions [56]

Before focusing on wall functions, it is fundamental to introduce two important quantities, which are the wall normal distance, y^+, and the dimensionless velocity, U^+, defined as follows:

$$y^+ = \frac{y u_\tau}{\nu} \tag{3.40}$$

and

$$U^+ = \frac{U}{u_t} \tag{3.41}$$

where u_t is a reference velocity computed from the wall shear stress, even because the velocity at the wall is zero due to the no-slip condition, introduced here:

$$u_t = \sqrt{\frac{\tau_w}{\rho}} \tag{3.42}$$

These non-dimensional quantities, usually referred at as wall units, are useful to compare different boundary layers. Given this definition, it is possible to introduce that all the boundary layers are similar if expressed in terms of wall units, showing the same behaviour; hence it is possible to define three regions of the boundary layer, characterized by a range of y^+: the viscous sub-layer, the buffer layer and the log-law region, or fully turbulent region. The viscous sub-layer is the region nearest to the wall, $y^+ < 5$ where viscous forces are dominant and shows a linear velocity profile (blue line in figure 3.3):

$$U^+ = y^+ \tag{3.43}$$

The buffer layer is the intermediate region, defined for $5 < y^+ < 30$, and no clear law, in terms of velocity profile, can be observed. The log-law region is defined for $y^+ > 30$ and here the velocity profile is logaritmic (green line in figure 3.3), as follows:

$$U^+ = \frac{1}{k}\log(Ey^+) \tag{3.44}$$

where k and E are empirical coefficients equal to 0.4187 and 9.793 respectively.

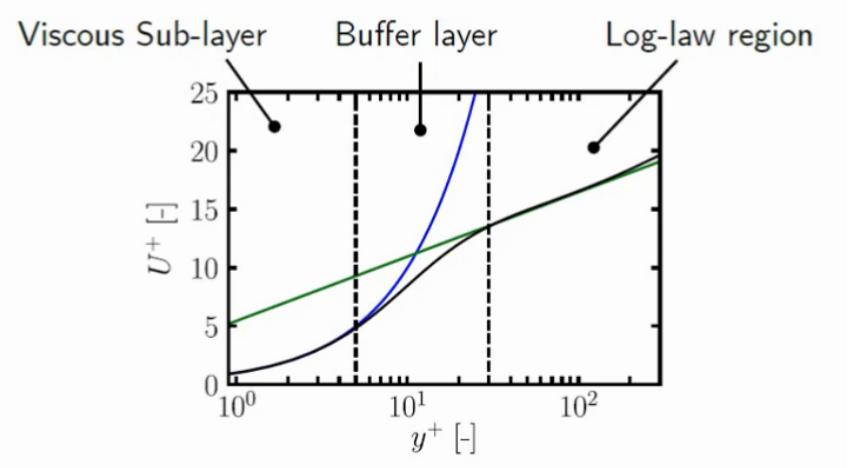

Figure 3.3: Boundary layer regions [56]

The black line in figure 3.3 represents the real behaviour of U^+ versus y^+ in the boundary layer and it is possible to see that in the viscous sub-layer region and in the log-law region the two velocity profile proposed are behaving accordingly to the experimental data. In practice wall functions express U^+ as a function of y^+ as follows:

$$U^+ = f(y^+) \tag{3.45}$$

Wall functions differ one from the other accordingly to the different representation of the function f; the shape of f can vary in the whole y^+ range. The last aspect that needs to be addressed is how wall functions work in practice; in order to explain this it is important to focus on a cell that is in contact with a wall. In the cell face that is attached to the wall the velocity is zero, due to the no-slip condition ,while at the centroid of the cell a certain velocity, U_p, is evaluated from the momentum equation. In general, the wall shear stress τ_w can be computed as follows:

$$\tau_w = -\rho\nu(\frac{\partial U}{\partial y})_{y=0} \tag{3.46}$$

Between different cells in a CFD mesh, the velocity profile is always considered as linear, so the wall shear stress results as follows:

$$\tau_w = -\rho\nu_w \frac{U_p}{y_p} \tag{3.47}$$

where ν_p is the effective kinematic wall viscosity and it has to be computed, taking into account the real velocity profile, in order to evaluate, with a linear velocity profile, the correct wall shear stress. In order to compute the effective kinematic viscosity ν_w, it is important to consider a certain velocity profile, expressed as in equation 3.21. The particular representation of the function is not important, but at the end of the section, some examples of function will be exploited. Recalling the definition of U^+, equation 3.17, it is possible to rewrite it:

$$U^+ = \frac{U}{u_t} = \frac{U u_t}{u_t^2} = \frac{U u_t \rho}{\tau_w} \tag{3.48}$$

then considering equation 3.21:

$$\frac{U u_t \rho}{\tau_w} = f(y^+) \tag{3.49}$$

then rearranging it:

$$\tau_w = -\frac{U_p u_t \rho}{f(y^+)} \tag{3.50}$$

By comparing this equation, representing the real wall shear stress, with the on for the wall shear stress in a CFD cell, equation 3.23, the effective kinematic wall viscosity ν_w can be evaluated:

$$\nu_w = \frac{y_p u_t}{f(y^+)} = \nu(\frac{y^+}{f(y^+)}) \tag{3.51}$$

The next step is to define some possible shapes of the velocity profile expressed in wall units.

Standard wall function

Standard wall function is used in mostly every CFD code and it is the simplest wall function available. In this case the velocity profile is a piecewise defined function; referring to the profiles highlighted above, in the section related to the boundary layers regions, the two profiles have an intersection for $y^+ = 11.25$ so for $y^+ < 11.25$ the function is:

$$U^+ = y^+ \tag{3.52}$$

while for $y^+ > 11.25$:

$$U^+ = \frac{1}{k}\log(Ey^+) \tag{3.53}$$

These wall function has a strong limitation, due to its definition, in the buffer region ($5 < y^+ < 30$), where the experimental trend differs significantly from the linear and the logaritmic profiles. The standard wall function is widely used in CFD but requires a mesh that shows values of y^+ either in the viscous sub-layer region or in the log-law region, for the problems explained above.

Blended wall functions

An alternative to the standard wall function is to consider a single smooth function valid through all the domain, $y^+ < 300$. For example, the Spalding's wall function can be used to fit with good approximation the real behaviour of the velocity profile in the whole boundary layer. The Spalding's wall function is defined as follows:

$$y^+ = U^+ + 0.1108[e^{0.4U} - 1 - 0.4U^+ - \frac{1}{2}(0.4U^+)^2 - \frac{1}{6}(0.4U^+)^3] \tag{3.54}$$

Most of CFD codes adopt singular wall functions blended between the viscous sub-layer region and the log-law region, in order to approach with higher accuracy the buffer region.

Enhanced wall function

Enhanced wall functions are used only in ANSYS Fluent to solve the boundary layer region. In this work this kind of function has been used so an overview on the differences with respect to standard wall functions is here proposed. The key aspect to be analyzed is that the enhanced wall functions differ from the standard wall functions for a different shape of $f(y^+)$; here follows its formulation:

$$f(y^+) = e^{\Gamma} u^+_{lam} + e^{\frac{1}{\Gamma}} u^+_{turb} \tag{3.55}$$

where:

$$\Gamma = \frac{-0.01(y^+)^4}{1 + 5y^+} \tag{3.56}$$

$$u^+_{lam} = y^+ \tag{3.57}$$

and

$$u^+_{turb} = \frac{1}{k} \log(Ey^+) \tag{3.58}$$

The blending functions are e^{Γ} and $e^{\frac{1}{\Gamma}}$, proposed by Kader in 1981, and allows to have a smooth function, valid in all the boundary layer region, that fits with good accuracy the velocity profile in the buffer region too, except for values of y^+ close to 5. In terms of CFD,

the actual outcome is a different formulation of the effective kinematic wall viscosity, that will be equal to:

$$\nu_w = \nu\left(\frac{y^+}{e^{\Gamma}u^+_{lam} + e^{\frac{1}{\Gamma}}u^+_{turb}}\right) \tag{3.59}$$

accordingly to the definition given in the previous section.

3.5. Species transport

Chemistry is of key importance while addressing a CFD simulation of a reactor. The final output of a reactor is achieving high conversion of the feed and, at the same time, high quantity of the desired species in the outlet flow. From a thermodynamic point of view, the thermal power required by the reforming reactions, that are highly endothermic, represents the majority of the total power exchanged in the reactor itself, as will be shown in the last chapter. For this reason, without having a too accurate prediction of the reactions kinetics, in this thesis work, reactions have been simulated to account for the thermal power required and to consider, approximately, the conversion of the feed, in order to estimate the overall quality of the process. In this section an overview on the equations and models, adopted to approach the chemistry of the problem, will be presented. In order to model, in a general CFD code and in particular in ANSYS Fluent, the mixing and transport of chemical species, conservation equation, considering convection, diffusion and sources term for every chemical species, must be solved. Furthermore it is possible to solve more than one reaction simultaneously with the same reactants/products. Before addressing directly the reaction problem it is important to consider the species transport modelling; in ANSYS Fluent, in order to predict the local mass fraction of all the species present in the flow, Y_i, a convection-diffusion equation for the i^{th} species must be solved. The equation is expressed as follows:

$$\frac{\partial}{\partial t}(\rho Y_i) + \nabla \cdot (\rho \boldsymbol{U} Y_i) = -\nabla \cdot \boldsymbol{J}_i + R_i + S_i \tag{3.60}$$

where the first three terms are the standard ones in transport equations (accumulation, convection and diffusion), the term R_i represents the net production of the i^{th} species due to reaction and the term S_i is a source or sink term defined by the user. Considering a flow in which N fluid phase chemical species are present, this equation must be solved for $N-1$ species; known the mass fractions of the i^{th} species, Y_i, the last one can be computed closing the summation of all the mass fractions that needs to result in unity. The term $\boldsymbol{J_i}$, that describes diffusion in equation 3.39, has different formulations if the flow is laminar or turbulent. Considered the problem in analysis and the conditions of

the flow of biogas in the reactants side, the laminar approach have been used and will be considered here. Here follows the formulation of $\boldsymbol{J_i}$:

$$\boldsymbol{J_i} = -\rho D_{i,m} \nabla Y_i - D_{T,i} \frac{\nabla T}{T} \tag{3.61}$$

3.5.1. Finite-rate chemistry

In order to close the conservation equation representing the species transport, equation 3.39, it is fundamental to consider models that can be used to address correctly the reactions occurring in the flow. Finite-rate kinetics, with no turbulence-chemistry interaction, allows to address problems in which turbulence is small or not presence, by neglecting the effect of turbulent fluctuations on kinetic and computing directly reaction rate by using general finite-rate chemistry. The production due to reaction of a general i^{th} species is the sum of the generation/consumption of the considered species by every reaction present in the system in which the i^{th} species participates. This production term can be evaluated as follows:

$$R_i = M_{w,i} \sum_{r=1}^{N_R} \hat{R}_{i,r} \tag{3.62}$$

where the summation is over all the reactions considered, $M_{w,i}$ is the molecular weight of the i^{th} species and $\hat{R}_{i,r}$ is the molar rate of creation/destruction of the i^{th} species in the r^{th} reaction. Considering the r^{th} reaction it is possible to express it in a general form:

$$\sum_{i=1}^{N} \nu'_{i,r} S_i \underset{\mathrm{k}_{b,r}}{\overset{\mathrm{k}_{f,r}}{\rightleftarrows}} \sum_{i=1}^{N} \nu''_{i,r} S_i \tag{3.63}$$

where N is the number of chemical species in the system, $\nu'_{i,r}$ and $\nu''_{i,r}$ are the stoichiometric coefficients of the i^{th} species respectively as reactant and product, S_i represents the generic chemical symbol denoting species i and $k_{f,r}$ and $k_{b,r}$ are the forward and backward rate constants for reaction r. The summations in equation 3.39 are for all chemical species in the system, but only species that appear as reactants or products will have nonzero stoichiometric coefficients. Stated the general form of a general reaction r, it is fundamental to evaluate its molar rate of production/destruction of an i^{th} species, as follows:

$$\hat{R}_{i,r} = (\nu''_{i,r} - \nu'_{i,r})(k_{f,r} \prod_{j=1}^{N} [C_{j,r}]^{\eta'_{j,r}} - k_{b,r} \prod_{j=1}^{N} [C_{j,r}]^{\eta''_{j,r}}) \tag{3.64}$$

where $C_{j,r}$ is the molar concentration of species j while $\eta'_{j,r}$ and $\eta''_{j,r}$ are the rate of exponent for reactant and product, respectively, species j in reaction r. These last two

terms are computed as the product of the stoichiometric coefficients, respectively, of the reactants and the products. In order to be able to evaluate the molar rate of production/destruction of an i^{th} species, the forward rate constant has to be computed; here follows its formulation:

$$k_{f,r} = A_r T^{\beta_r} e^{-\frac{E_r}{RT}} \tag{3.65}$$

where A_r is the Arrhenius constant, β_r is the temperature exponent and E_r is the activation energy; these terms are referred to a particular reaction r and have to be inserted manually by the user, as will be shown in the next chapter. Considering reversible reaction, the backward rate constant has to be evaluated by using the equilibrium constant, K_r:

$$k_{b,r} = \frac{k_{f,r}}{K_r} \tag{3.66}$$

The equilibrium constant needs to be evaluated considering this formulation:

$$K_r = \exp(\frac{\Delta S_r}{R} - \frac{\Delta H_r}{RT})(\frac{p_{atm}}{RT})^{\sum_{i=1}^{N}(\nu''_{i,r} - \nu'_{i,r})} \tag{3.67}$$

The term within the exponential function represents the change in Gibbs free energy, and its components are computed as follows:

$$\frac{\Delta S_r}{R} = \sum_{i=1}^{N}(\nu''_{i,r} - \nu'_{i,r})\frac{S_i}{R} \tag{3.68}$$

$$\frac{\Delta H_r}{RT} = \sum_{i=1}^{N}(\nu''_{i,r} - \nu'_{i,r})\frac{h_i}{RT} \tag{3.69}$$

where S_i and h_i are the entropy and enthalpy values of the species i evaluated at temperature T and atmospheric pressure and must be given by the user.

3.5.2. Relax to chemical equilibrium

In the Relaxation to Chemical Equilibrium model, the species composition is brought to its equilibrium state. The reaction source term in the average i^{th} species conservation equation is modeled as follows:

$$R_i = \rho\frac{Y_i^{eq} - Y_i}{\tau_{char}} \tag{3.70}$$

where Y_i^{eq} is the mass fraction at the equilibrium and τ_{char} is a characteristic time. Equation 3.69 suggests that species undergo reactions towards their chemical equilibrium state over a characteristic time period, τ_{char}. As chemical equilibrium is not influenced by reac-

tions or reaction rates, the reaction source term in Equation 3.69 remains unaffected by the reaction mechanism for a given τ_{char} value. In cases where no turbulence-chemistry model is employed, the characteristic time is determined through the following calculation:

$$\tau_{char} = \tau_{conv} + \tau_{chem} \tag{3.71}$$

where τ_{conv} is a convection/diffusion time-scale in a cell. The other quantity is instead computed as:

$$\tau_{chem} = min_f(\frac{Y_f}{\frac{dY_f}{dt}}) \tag{3.72}$$

where the subscript f refers to all the species present in the reaction.

4 | CFD simulation setup

In this chapter, the actual geometry considered, the mesh adopted to discretize the indirect heated reformer and the setup chosen, in terms of models, boundary conditions and both fluid and solid properties, will be presented while the reasons behind the choices will be highlighted and explained.

4.1. Meshing

The precise definition of the geometry used to simulate the behavior of the indirect heated reformer is crucial, as it differs from the overall geometry presented in Chapter 2 and depicted in Figure 2.1. It is important to note that the simulation was conducted on only a part of the complete 3D mesh in order to decrease the size of the control volume and reduce computational power required and simulation time. However, it should be emphasized that the geometry was truncated due to its symmetry. Previous simulations on this reformer used a 2D mesh, because the studied geometry showed a radial symmetry, due to the absence of baffles, which allows to achieve convergence in just a few minutes. This thesis builds on that previous work by studying the effect of introducing baffles. However, the introduction of spider baffles eliminates the radial symmetry of the geometry, creating a more complex scenario. Nevertheless, as seen in Figures 2.4 and 2.6, the geometry retains symmetry every 120°, allowing it to be cut into three parts, with each part shown in the subsequent figures. It is essential to clarify why the solid body representing the reactor shell is not visible in the figures. The reactor shell has been modeled directly in ANSYS Fluent using a wall-type boundary condition applied to the outer surfaces of the heat transfer fluid and baffles. However, the heat transfer fluid is not visible in these figures to provide a clearer view of the geometry. The key importance aspects to emphasize include the dimensions of the reformer unit. The length of the reactor is measured in the y-coordinate of the Cartesian system and is 3 meters long. The inner diameter of the shell, which corresponds to the diameter of the inlet for the heat transfer fluid, is 23.2 cm, resulting in an inlet area of 422.65 cm^2. It is worth noting that the internal bayonet-tube is shorter than the shell, measuring 2.58 m in length. The bayonet-tube has

an inlet diameter of 13.57 cm, and its total area is 144.67 cm^2. This portion is utilized by both the annular biogas inlet, which has an area of 135.98 cm^2, and the syngas outlet, which only occupies a small area of 7.06^2 cm^2. The total internal area of the bayonet-tube is not equivalent to the sum of the inlet and outlet surfaces because of the presence the internal tube of the bayonet configuration. The geometry of the reactor is composed of 11 domains, which can be categorized into solid and fluid domains. Among the 11 domains, 7 are solid domains, which include the 5 baffles and the 2 tubes (inner and outer) of the bayonet-tube. On the other hand, the fluid domains consist of 4 parts. One is the heat transfer fluid side, which contains superheated steam, and the remaining three are the biogas/syngas domains, which are further divided into two different syngas domains and one reactants domain. This division into three parts has two reasons. Firstly, it simplifies the creation of fluid domains inside the initial CAD geometry. Secondly, the reactions occur only in the first portion of the bayonet-tube, where the catalyst is present, and not in the remaining parts of the biogas domain. After adequately characterizing the geometry of the reformer, the focus can now shift to the mesh used for simulations. Three distinct meshes have been employed to simulate the reactor's behavior with the three geometries considered: the plain tube geometry, which is without baffles, and the two geometries with baffles, with one having a baffle radial gap of 10 mm, and the other having baffles with a radial gap of 20 mm. Additionally, it is essential to note that to ensure simulation results are not dependent on a specific mesh, a mesh independence study must be performed. In this thesis, a mesh independence study has been conducted on the 20 mm radial gap baffles geometry since the mesh can significantly impact the flow simulation due to the strong restriction imposed by the small radial gap of the baffles. A well-constructed mesh is necessary in the region between the baffles and bayonet-tube to capture the flow behavior correctly. For the mesh independence study, that will be shown in Chapter 5, for the above mentioned geometry, three different meshes have been considered. The meshes used for the simulations were created with ANSYS Meshing, a tool available in ANSYS Workbench. ANSYS Meshing have been used to generate the meshes, by imposing an average cell size as input. No inflation layers have been used, which allowed for a structured mesh in the simpler domains, such as the reactants and syngas domains, and helped to achieve better convergence in these regions. Unstructured meshes, especially in the syngas domain, were prone to issues related to reverse flow. The zones near the baffles have been refined directly in ANSYS Fluent to have a finer mesh in the areas that are the most relevant for the study, due to the strong presence of turbulence. The topology of the three meshes, done on the geometry with 10 mm radial gap baffles, adopted to carry out the mesh independence study, is similar, with the only difference being the element size. The element size have been gradually decreased from

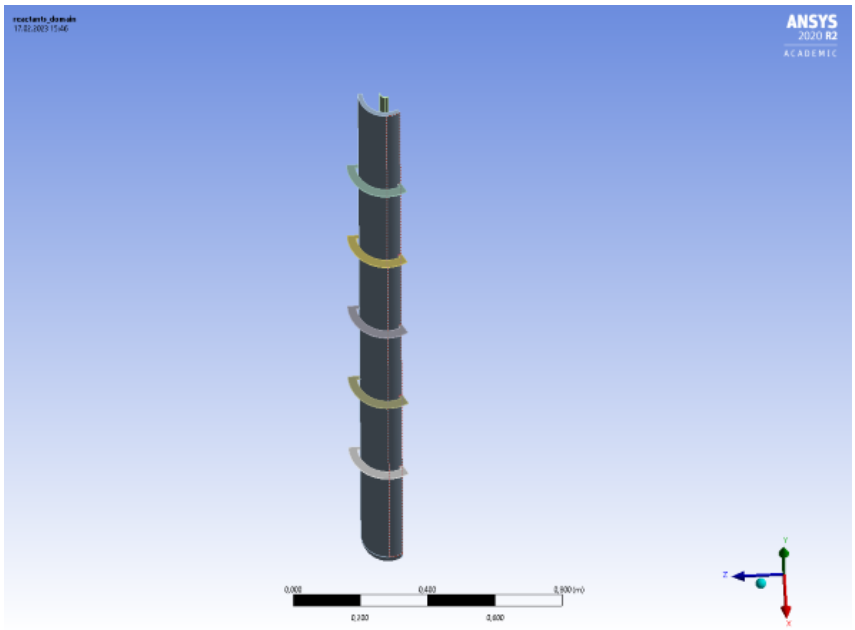

(a) Side view

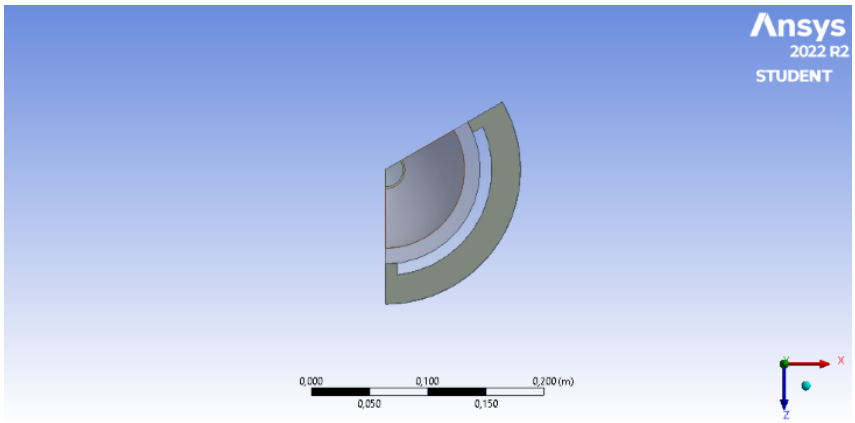

(b) Top view

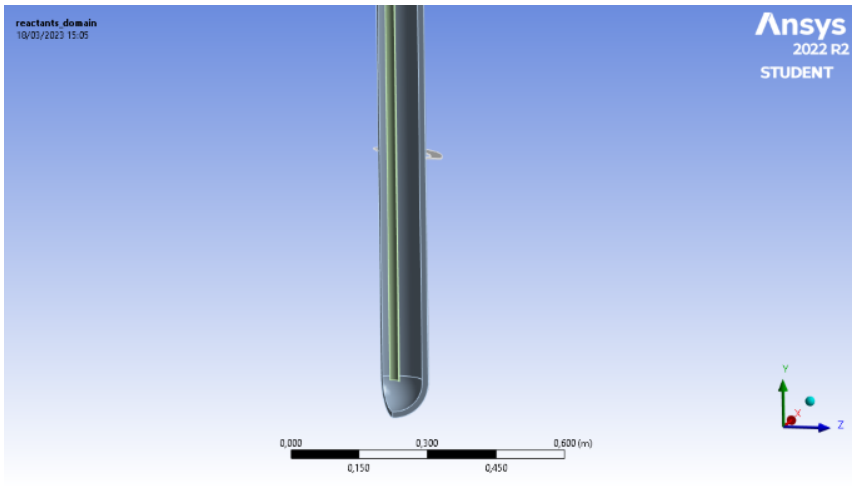

(c) Bayonet-tube: particular

Figure 4.1: Cut reformer geometry views

0.005 m to 0.004 m and then to 0.0035 m during the mesh independence study, resulting in meshes with 1′622′159, 2′884′495, and 4′111′970 cells, respectively. The meshes for the plain tube and the baffle with an air gap of 20 mm shear the topology with the meshes of the first geometry considered and only the two lowest element sizes have been used. It is important to note that the finest mesh was used when simulating the reactor behavior without radiation, while the intermediate mesh was used when radiation was included. This was done to reduce computational time, which would have been otherwise unsustainable.

4.2. Materials

The accurate characterization of the materials, including their composition and rheological properties, is crucial when conducting CFD simulations of this nature. Such information can significantly affect the reactor's physics, including mass flow rate, thermal power exchange, and pressure drops. Therefore, a dedicated section will be allocated to define the materials utilized in this problem, by dividing them into fluids and solids.

4.2.1. Fluids

The reformer analyzed in this thesis contains two zones filled with fluid flows. The first domain is located between the shell and the outer tube of the bayonet-tube, where the heat transfer fluid flows. The second zone, inside the bayonet-tube, contains biogas and is divided into three parts as explained in the previous section. The heat transfer fluid, which is superheated steam consisting of only H_2O, has been studied initially. Its properties such as density (ρ), specific heat (c_p), thermal conductivity (k), and viscosity (μ) have been defined for a temperature range between $800K$ and $1225K$ since the superheated steam enters the reformer with an inlet temperature of 1223.15 K and at atmospheric pressure. The data related to the fluid properties have been obtained from the National Institute of Standards and Technology (NIST) database to ensure accuracy. As the temperature varies significantly for both fluids in this application, while pressure shows small variations with respect to the operative one, a polynomial interpolation has been used to consider the variable properties with respect to temperature. The interpolation includes quadratic and linear expressions, depending on the quality of the fitting. Superheated steam properties are interpolated for a temperature range of $800K$ to $1225K$, ensuring reliability only within this range, which covers the behaviour of the variable, for the steam, along the entire reformer length. To avoid early divergence issues during the initial iterations of a simulation, constant fluid properties have considered before introducing variable

properties. Moving on to the reaction side, it is important to note that the biogas composition of the bayonet-tube reformer comprises methane (CH_4), carbon dioxide (CO_2), water (H_2O), and nitrogen (N_2). However, the mixture must also consider hydrogen H_2 and CO, which are the products of the reforming reactions occurring inside the reformer. The properties of the reactants species have been obtained from NIST and interpolated within the operating range, with notable differences concerning the pressure. The reactants operate at a pressure of 10 bar, thus properties for the actual pressure must be used. Additionally, the biogas inlet temperature is $773.15K$, and therefore, the properties were interpolated in a temperature range of $T = 700K$ to $T = 1250K$ to ensure accuracy across the entire operating range. In ANSYS Fluent the mixture properties are evaluated using specified mixing laws of the properties of the species present in the mixture. The formulations adopted to evaluate the properties of the mixture are expressed as follows:

$$\rho_{mix} = \frac{1}{\sum_i^{N_s} \frac{Y_{i=1}}{\rho_i}} \tag{4.1}$$

$$c_{p,mix} = \sum_i^{N_s} c_{p,i} Y_i \tag{4.2}$$

$$k_{mix} = \sum_i^{N_s} k_i Y_i \tag{4.3}$$

and

$$\mu_{mix} = \sum_i^{N_s} \mu_i Y_i \tag{4.4}$$

4.2.2. Solids

The present thesis work involves the consideration of two solids in the reformer, which are steel and aluminum-silicate-alsitra-1400. Due to the relatively low expected variation of the properties of these materials with respect to temperature, the properties have been assumed to be constant in the temperature range of interest. The properties for steel, including density, specific heat, and thermal conductivity, have been directly obtained from the ANSYS Fluent database. For aluminum-silicate-alsitra-1400 the properties were available from a previous 2D study carried out on the same reactor.
Steel properties:

- Density: $\rho = 8030\ \frac{kg}{m^3}$
- Specific heat: $c_p = 502.48\ \frac{J}{kgK}$

- Thermal conductivity: $k = 16.27\ \frac{W}{m^2K}$

Aluminum-silicate-alsitra-1400 properties:

- Density: $\rho = 128\ \frac{kg}{m^3}$
- Specific heat: $c_p = 840\ \frac{J}{kgK}$
- Thermal conductivity: $k = 0.11\ \frac{W}{m^2K}$

It is worth noting the relatively low thermal conductivity of aluminum-silicate-alsitra-1400, which explains why it was selected as the insulating material. The effects of this choice will be illustrated in the upcoming chapter when analyzing the thermal power exchanged with the surroundings.

4.3. Model selection

This section will highlight the models utilized for conducting the simulations, assuming that the underlying theory of these models has already been extensively elaborated. The simulations have been executed adopting the pressure-based solver, as the flows inside the reformer are not highly compressible, which is evident from the inlet velocities of the two fluids. Additionally, the coupled pressure-velocity coupling technique has been employed due to the substantial computational power available on the simulation computer. This method facilitates quicker convergence in comparison to a segregated algorithm.

4.3.1. Turbulence model

Turbulence in the simulations has been modeled using the $k - \epsilon$ realizable model, as it is the most robust and suitable for addressing such problems. In fact, most of the CFD simulations on heat exchangers with baffles in the literature adopt this model. For completeness, in the first simulated case involving the reformer with 10 mm radial gap baffles, the $k - \omega$ SST model have been also adopted to compare the results between the two models. For the realizable $k - \epsilon$ model the enhanced wall treatment has been chosen to model the boundary layer due to the y^+ values at the wall obtained during the simulations, as will be shown in Chapter 5.

4.3.2. Reactions

In the reformer simulated in this thesis work, as anticipated in Chapter 2, three different reactions have been considered in the biogas side, which are:

- Steam reforming: $CH_4 + H_2O \rightleftharpoons 3\,H_2 + CO$
- Dry reforming: $CH_4 + CO_2 \rightleftharpoons 2\,H_2 + 2\,CO$
- Water gas shift: $CO + H_2O \rightleftharpoons CO_2 + H_2$

These three reactions have been considered and simulated simultaneously during the simulations and, to be determined, some values from the literature have been taken, such as activation energy E_r, Arrhenius constant A_r and temperature exponent β_r, as explained in the dedicated section. The values adopted for the reactions present in the reformer are:

- Steam reforming: $A_r = 1.17e^{+12}$, $E_r = 2.401e^{+08}\frac{J}{kgmol}$, $\beta_r = 0$
- Dry reforming: $A_r = 8.31e^{+09}$, $E_r = 6.65e^{+07}\frac{J}{kgmol}$, $\beta_r = 1$
- Water gas shift: $A_r = 543$, $E_r = 6.713e^{+07}\frac{J}{kgmol}$, $\beta_r = 0$

The backward reactions have been included. For what regard the kinetic of the reactions, the model adopted in this work, the relax to chemical equilibrium, considers the reaction at equilibrium, as explained in the relative section. This kind of simplification is adopted because the main aim of this work is to understand the effects of the baffles on turbulence and heat transfer, while a precise evaluation of the chemistry is not required, due to the early stage of the project.

4.3.3. Radiation

The radiation has been simulated using the Discrete Ordinates model with a highly precise angular discretization, taking into account both N_{theta} and N_{phi} with a value of 5. As for the wavelengths and the properties of absorbivity, emissivity, and scattering coefficient of the heat transfer fluid, a user defined function has been adopted, which selects realistic values for these properties depending on the wavelength. However, since this function is protected, it is not possible to delve further into how it works.

4.4. Boundary conditions

In this section, the boundary conditions applied to setup the simulations in ANSYS Fluent will be presented, giving, where is necessary, clarifications about the choices adopted.

4.4.1. Inlet

In the considered reformer geometry, two different fluids are present, superheated vapor and biogas, and so two different inlet boundary conditions have been used. Both boundary

conditions are velocity-inlet; hence the key parameter to define is velocity. The velocity profile is considered as normal to the boundary surface and only the magnitude of this parameter needs to be setup by the user. Other two parameters are requested, the inlet static temperature and the gauge pressure. These three input are considered differently by the software, in fact both the inlet velocity and temperature are fixed by the input parameter, while the indication on pressure is a guess pressure that during the simulation usually is not met, it is needed to have a starting point. This fact is related to the outlet boundary condition that has been chosen and, for this reason, this aspect will be explained later in this section. Focusing on the actual parameters given as an input, the static temperatures for the two fluids, as already mentioned, are $T = 1223.15K$ and $T = 773.15K$ respectively for the superheated vapor and the biogas. Before giving the velocity magnitude, is important to underline that the real boundary condition is the mass flow rate, which is a constraint, but a velocity-inlet boundary condition is being preferred because is better digested by the software, due to the possibility of having as an input the static temperature while in the mass flow rate inlet, the total temperature is the requested parameter; hence the velocity magnitude has been artificially computed, knowing the density at the inlet of both superheated vapor and biogas, by using the definition of the mass flow rate:

$$v_{in} = \frac{\dot{m}}{\rho A_{in}} \tag{4.5}$$

being the inlet section given from the geometry and the density fully determined when the temperature is known. In particular the two velocity magnitudes are $v_{in,htf} = 5.5417$ m/s and $vin, bio = 0.2944$ m/s, defined in order to met the two target mass flow rate of $\dot{m}_{in,htf} = 0.042$ kg/s and $\dot{m}_{in,bio} = 0.01478$ kg/s. It is important to notice that the mass flow rate of the heat transfer fluid is almost three times the biogas one. The last thing that needs to be underlined is that the reported mass flow rate are referred to the whole reactor, while in the CFD simulations, the mass flow rate, as every other extensive property, are $\frac{1}{3}$ of the actual one because only $\frac{1}{3}$ of the total reactor has been simulated, due to the symmetry properties of the geometry. For what regards the biogas side, it has been necessary to insert in the velocity-inlet boundary condition, the inlet composition of the biogas, which is expressed in mass fractions, as follows: $Y_{\mathrm{CH_4}} = 0.167$, $Y_{\mathrm{CO_2}} = 413$, $Y_{\mathrm{H_2O}} = 0.375$ and $Y_{\mathrm{N_2}} = 0.045$.

4.4.2. Outlet

The outlet boundary conditions considered in this simulations are two, one for the heat transfer fluid side and one for the reactants side. The boundary conditions chosen in both cases are pressure-outlets. The pressure outlet is completely defined by inserting

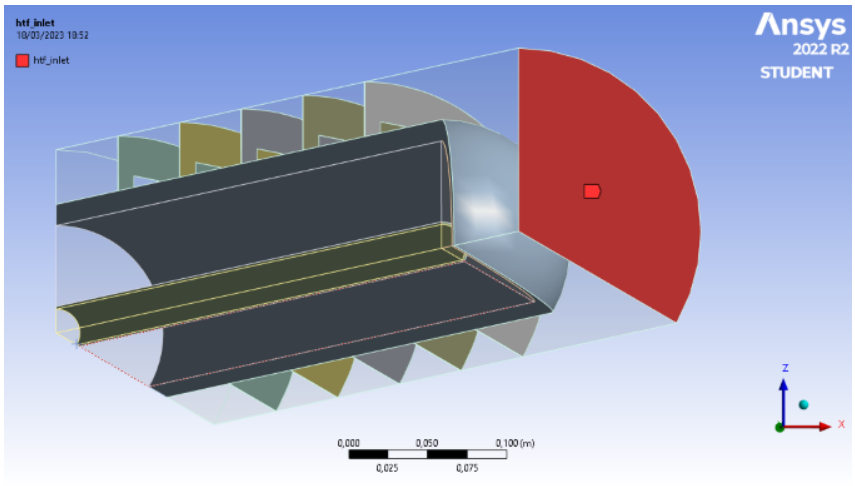

(a)

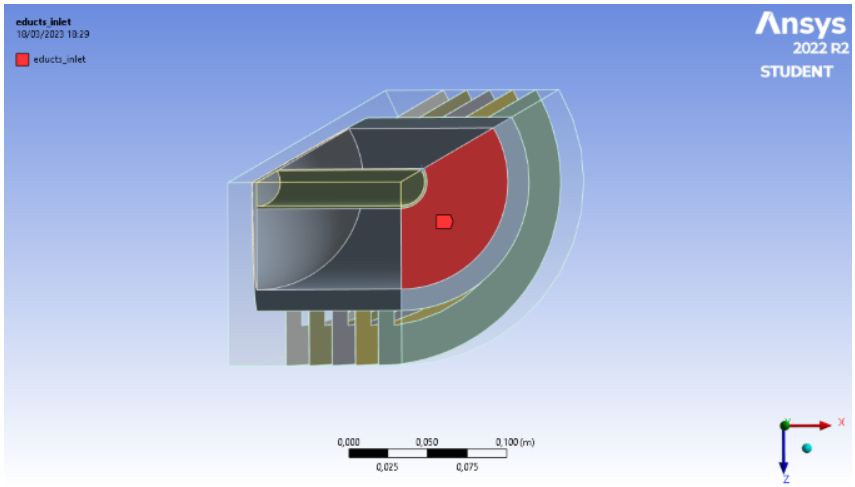

(b)

Figure 4.2: Inlet boundary conditions

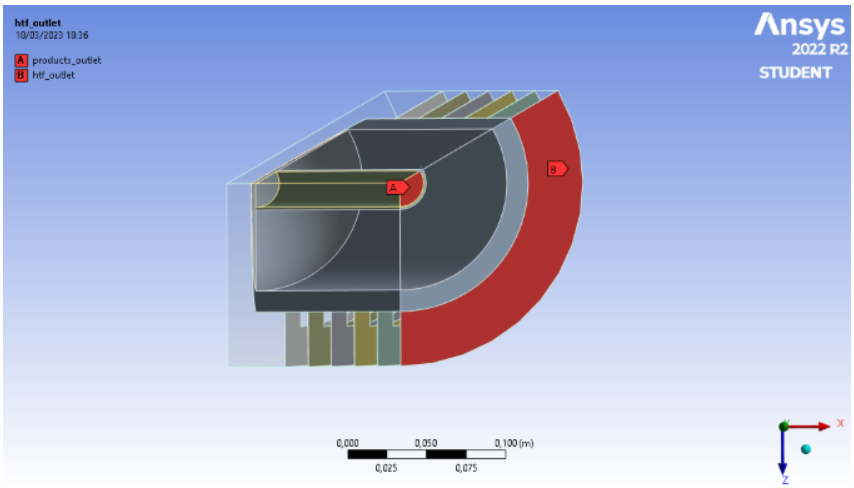

Figure 4.3: Outlet boundary conditions

the gauge pressure of the flow considered. It is important to underline that in ANSYS Fluent the operative pressure is defined in the reference values, which in this case is the atmospheric pressure $P_{atm} = 101325\ Pa$, and so in the pressure outlet, it is specified the difference between the reference pressure and the actual pressure of the flow at the outlet. Focusing on the values used in this simulations, the gauge pressures are $P = 0$ and $P = 858675\ Pa$, because the heat transfer fluid is considered at atmospheric pressure at the outlet while the syngas is at a pressure $P = 10\ bar$ at the inlet of the reactor, and with the pressure drops from the inlet to the outlet, a near value is reached.

4.4.3. Symmetry

The symmetry boundary condition in applied when the physical geometry of interest, and the expected pattern of the flow and thermal solutions, behaves like a mirror. In particular ANSYS Fluent imposes a zero normal velocity and a zero normal gradients of all the variables at the symmetry plane. In the geometry studied in this thesis work, this type of boundary condition, is applied to all the faces resulted when the whole 3D geometry has been cut in three parts, due to the symmetry intrinsic in the geometry.

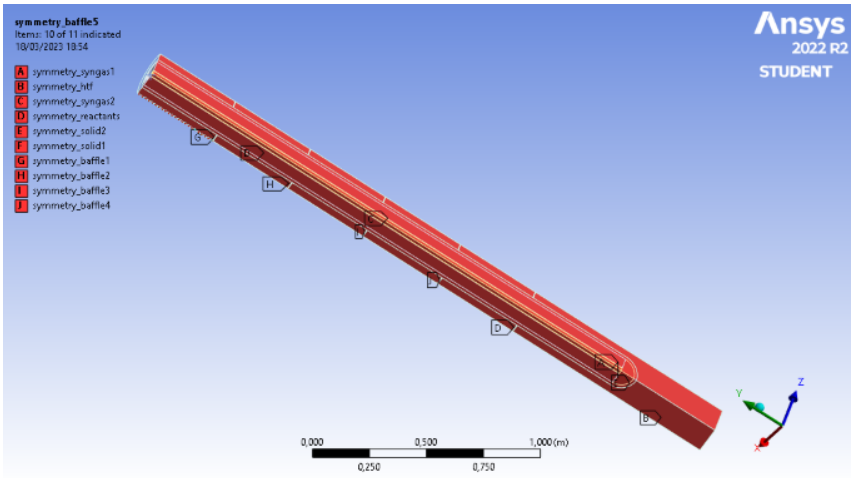

Figure 4.4: Symmetry boundary conditions

4.4.4. Walls

The walls present in the geometry of the reactor have been modelled as a wall-type boundary condition, but it is possible to divide between two categories of walls, depending on the position occupied in the geometry. While modelling wall-type boundary condition, in this work, thermal and radiative boundary conditions need to be considered. First of all it is important to underline that, except for the shell, all the other walls and baffles are made of steel. The first type of walls on which it is important to focus are the surfaces that are in the extreme border of the mesh. On this walls, in the boundary condition the heat transfer mechanism with the surroundings have been imposed. In particular, at the surfaces that represent the shell of the reactor, a convective heat transfer mechanism has been imposed and the material chosen is aluminum-silicate-alsitra-1400, an insulating material to reduce the heat transfer with ambient. The values requested to model this kind of boundary condition are the external heat transfer coefficient, the external temperature, and the wall thickness, which are respectively $h_{ext} = 15\ W/m^2K$, $T_{ext} = 300\ K$ and $t = 0.5m$. While the thickness is the actual thickness of the shell of the reactor, the other two values are standard reference values while considering natural convection with ambient. These values are not too accurate because, as it will be shown in the next chapter, the thermal power exchanged with ambient is a really small quantity, that can almost be neglected, due to the presence of the insulating layer at the shell. The other walls present at the border of the mesh are on the top and on the bottom of the mesh and are in particular the top faces of the inner and outer reformer tube. This walls have a quite small surface and in this case a zero heat flux has been imposed as boundary condition. On the other hand, all the surfaces that are in the internal part of the reactor,

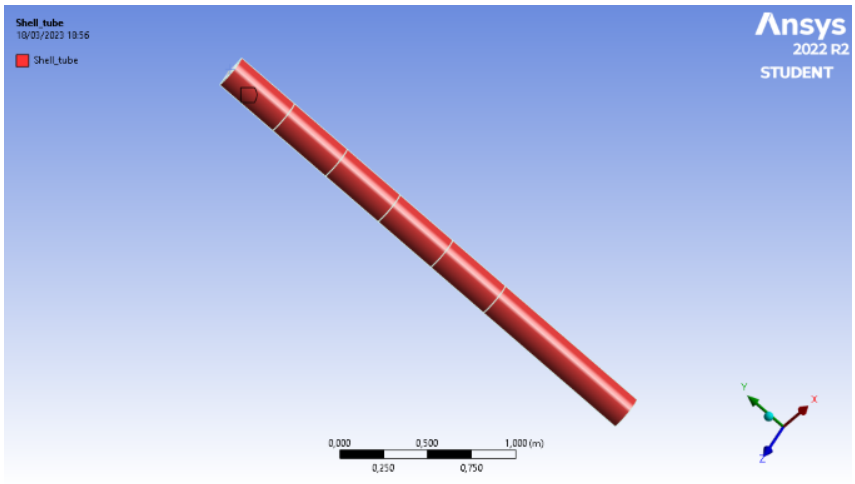

(a)

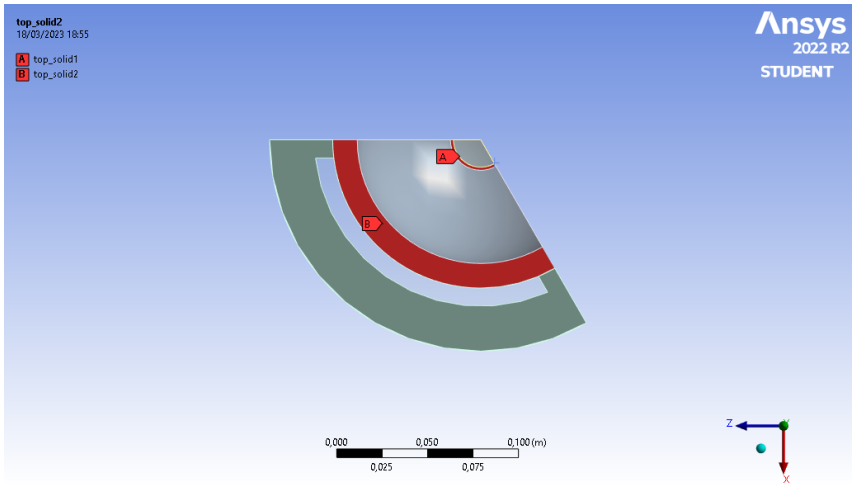

(b)

Figure 4.5: Wall boundary conditions

which are all the surfaces of the baffles, the lateral surfaces of the reformer tube and the internal face of the shell, have been modelled as thermally coupled. This modelling results in no further input requested because the solver calculates heat transfer directly from the solution in the adjacent cells, once the material of the wall has been specified. The last important thing that has to be highlighted is that in all the walls which are in contact with a fluid, the no-slip condition has been imposed, being a stationary wall.

5 | CFD simulation results

This chapter presents the results of the CFD simulations conducted on ANSYS Fluent for the bayonet-tube biogas reformer. The first section analyzes the mesh independence study, performed on the geometry including baffles with 10 mm radial gap. In the second section, a comparison between the $k-\epsilon$ and the $k-\omega$ turbulence models on the same geometry is presented, highlighting the differences in the turbulence quantities. The third section compares the three geometries considered in this thesis work: two geometries with baffles characterized by different radial gaps and one without baffles. Heat transfer properties are compared for these geometries without considering the radiative contribution. Finally, the last section studies the two geometries with baffles, considering radiation, evaluating its contribution and performing an analysis on the quality of syngas produced and the performances of the reformer.

5.1. Mesh independence study

The mesh independence study is a fundamental part of every CFD simulation, as it plays a crucial role in validating the accuracy of the results obtained. The purpose of the mesh independence study is to demonstrate that the results obtained through CFD simulations are not dependent on the mesh adopted. If the solution of the problem changes when modifying the mesh, the obtained results are inaccurate. In this thesis work, the reformer geometry with spider baffles, characterized by a radial gap of 10 mm, has been discretized into three different meshes to perform the study about the mesh independence. Although the meshes are similar in terms of topology, spatial distribution, and cell type, the mesh becomes finer from the first to the last one. These are the key values to consider in order to describe these meshes:

1. First mesh: $D_{avg} = 0.005\ m$, $N_{cells} = 1'622'159$
2. Second mesh: $D_{avg} = 0.004\ m$, $N_{cells} = 2'884'495$
3. Third mesh: $D_{avg} = 0.0035\ m$, $N_{cells} = 4'111'970$

where D_{avg} is the average element size that characterizes the cells of the mesh. The first

important aspect to consider is the convergence process in the three cases. For the first and second meshes, a boundary condition needs to be imposed to prevent reverse flow at the heat transfer fluid outlet, in order to allow the simulation to achieve convergence. This reverse flow is due to an inaccurate solution of the turbulent flow downstream the last baffle. The reverse flow prevention creates in all outlet cells, where the flow enters the system instead of exiting it, fictitious wall boundary conditions. This is a simulation issue, and, after a few iterations, the reverse flow has been eliminated even switching off the reverse flow prevention option. However, this indicates that these meshes are not fine enough to accurately evaluate the heat transfer fluid flow in this region of the domain. On the other hand, the third mesh showed no reverse flow issues, making it the best mesh of the three. Nonetheless, this reasoning alone is insufficient to determine if the solution is independent of the mesh. The obtained results must be presented and compared to establish the solution independence with respect to the mesh. The first method adopted to compare the results has been considering the variation of the main dependent variables, in particular the temperature, in the heat transfer fluid domain. Here follows the results for the three considered meshes:

	$T_{htf,out}[K]$	$\Delta T_{htf}[K]$	$\Delta P_{htf}[Pa]$	$Q_{htf,bio}[W]$	$Q_{amb}[W]$
1^{st} **mesh**	961.47	261.68	1448.3	25'468	388.8
2^{nd} **mesh**	986.91	236.24	1511.1	23'032	394.17
3^{rd} **mesh**	986.21	236.94	1563.2	23'097	394.11

Table 5.1: Mesh independence: outlet parameters

From Table 5.1, it is evident that the second and third meshes produce similar results in terms of temperature and pressure at the boundaries, overall thermal power exchanged with the biogas side ($Q_{htf,bio}$) and thermal power exchanged with the ambient (Q_{amb}). In contrary, the first mesh, which is the coarsest, leads to significant deviations compared to the other two cases. This deviation indicates that the results obtained using the first mesh are highly dependent on the mesh itself, making it unreliable for further analysis. It is important to recall that the extensive values reported in the table and in general reported in this thesis work, are considered for the complete 3D geometry. It is interesting to see how the different meshes predict the turbulence downstream the baffles. Due to the fact that being the first one, its effect are the most evident between the five present, the turbulence kinetic energy magnitude field downstream the first baffle is shown in figure 5.1, for the three different meshes considered. It is important to underline that, being the mesh 3D, the representation of the results is quite difficult and for this reason, a plane,

which is in the middle of the 3D geometry considered, will be used to show some key aspects and the profile of the variables in the reactor.

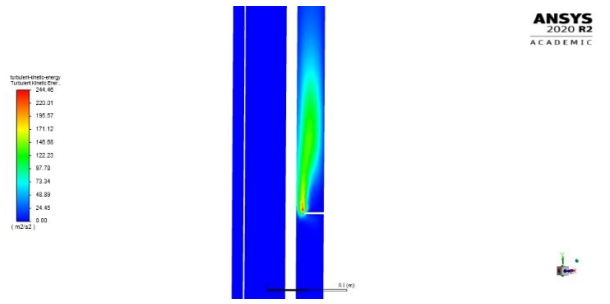

(a) First mesh.

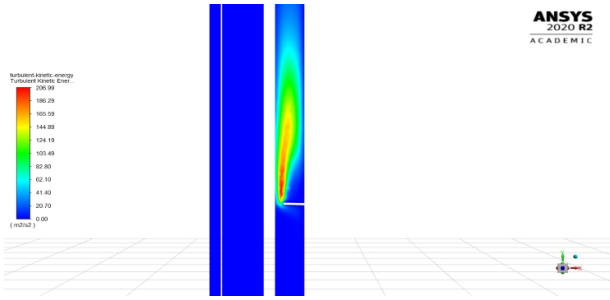

(b) Second mesh.

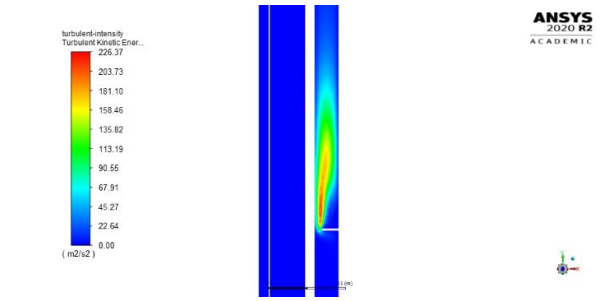

(c) Third mesh.

Figure 5.1: Mesh independence: turbulent kinetic energy

The figures presented provide evidence that the second and third meshes give similar results when simulating turbulence downstream the first baffle, while the first mesh produces significantly different results. The mesh independence study conducted in this section has important implications for selecting the appropriate mesh for subsequent simulations. The first mesh is unreliable and must be avoided, while the other two meshes are reliable and can be used for further simulations. The second mesh is preferred for simulating cases with radiation because it requires less computational power and time, despite yielding less accurate results. On the other hand, the third mesh is more suitable for cases in which the radiative heat transfer is not considered, because higher accuracy can be achieved

with the highest number of cells without significantly increasing computational power.

5.2. Turbulence models comparison

In this section a comparison between the two main available models considered in order to address turbulence for the simulation of the reformer behaviour will be presented. In particular the two models are the realizable $k-\epsilon$ model and the $k-\omega\ SST$ model, both of them being already deeply discussed in the dedicated chapter about CFD modelling. In order to make this comparison, the same geometry discussed in the last section has been used and the mesh adopted is the finest one, because radiative heat transfer is not considered in this study. The comparison is carried out considering the main output parameters and variables that characterize the heat transfer fluid domain, being turbulent fundamental while addressing the flow in this side of the reformer. In table 5.2 the outlet parameters, obtained as results for the simulations with the two different models, are highlighted:

	$T_{htf,out}[K]$	$\Delta T_{htf}[K]$	$\Delta P_{htf}[Pa]$	$Q_{htf,bio}[W]$	$Q_{amb}[W]$
$k-\epsilon$	986.21	236.94	1563.2	23'097	394.11
$k-\omega\ SST$	991.41	231.66	1575.7	22'526	397.83

Table 5.2: Turbulence models: outlet parameters

As it is possible to notice, there are some differences between the two solutions while adopting the same mesh but two different turbulence models. The key output value that has to be considered is the thermal power exchanged between the heat transfer fluid and the biogas side, which is $Q_{htf,bio}$. The absolute difference between the two values is 571.83 W, while the most effective parameter that needs to be accounted for,in order to describe the effective difference between the two approaches, is the percentage error, considered as:

$$e_{\%} = \frac{Q_{htf,bio,\epsilon} - Q_{htf,bio,\omega}}{Q_{htf,bio,\epsilon}} \cdot 100 \tag{5.1}$$

which is equal to 2.47 %, a perfectly fine deviation, considering that two strongly different models are being considered. In order to better compare the two model, it is necessary to consider the prediction of the turbulent kinetic energy magnitude downstream, for example, the first baffle. This aspect is shown in figure 5.2. It is possible to notice that the turbulent kinetic energy results are strongly different between the two simulations with different models. In order to give an explanation to this behaviour it is necessary

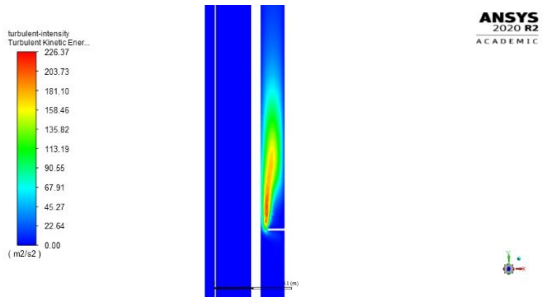

(a) Turbulent kinetic energy of $k - \epsilon$

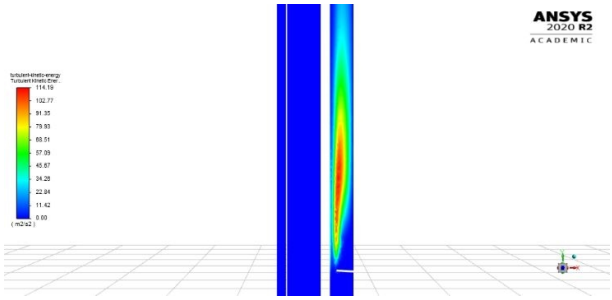

(b) Turbulent kinetic energy of $k - \omega$

Figure 5.2: Turbulence models: turbulent kinetic energy

to compare the y^+ values of the two cases, for the surface between the heat transfer fluid and the outer wall of the reformer tube, which is the most important zone while dealing with turbulence. The values of y^+ on the above mentioned surface are shown in figure 5.3. First of all it is important to recall that the y^+ values are not a characteristic of the mesh itself but are dependent on the flow predicted during the simulation, as it can be noticed here, in fact the meshes are equal. The second aspect to be underlined is that the realizable $k-\epsilon$ model, with the enhanced wall function, is capable of reaching good results even in the buffer layer, having really high accuracy in the viscous sub-layer region, with only some inaccuracy for values of y^+ near to 5. On the other hand the $k-\omega$ SST model is really accurate for values of y^+ that belong to the viscous-sub layer, while in the buffer region, some inaccuracies are present even if it adopts a blend between the standard $k-\omega$ model and the standard $k - \epsilon$ model. This fact is the reason for the deviation shown in predicting the turbulent kinetic energy in the zone downstream the baffles, where in fact there is the buffer region. On the other hand, the output values of interest for this thesis work, which are the heat transfer rates in the reformer, show a small relative deviation, as shown above, which is important to be underlined.

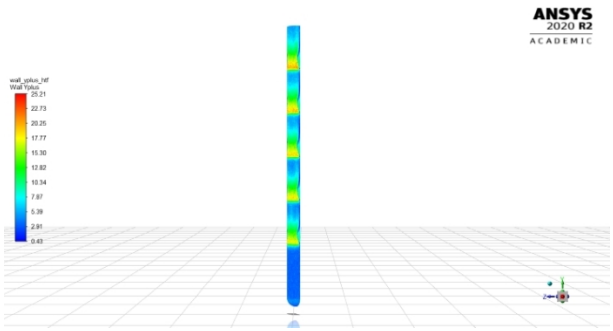

(a) y^+ of $k-\epsilon$

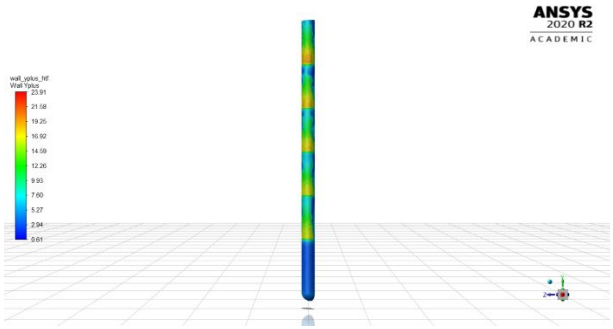

(b) y^+ of $k-\omega$

Figure 5.3: Wall units turbulence model

5.3. Baffles effect on convective heat transfer

In this section, a comparison between the three different geometries will be performed. In particular the radiative heat transfer will be neglected, in order to completely focus on the effect of the introduction of baffles, and only the heat transfer fluid side will be considered. Both the radiative heat transfer and biogas side will be analyzed in the next section. As already underlined, the meshes adopted for the other two geometries, the one with the baffles with 20 mm air gap and the one without baffles, are completely similar, in terms of cells type, dimensions and disposition in space to the third mesh presented in the first section of this chapter. The turbulence model considered here is the realizable $k-\epsilon$ model with the enhanced wall function. Recalling that the inlet temperature of the heat transfer fluid is 1223.15 K, the outlet values of the dependent variables of the heat transfer fluid domain and the thermal power exchanged by this fluid are shown in the following table:

	$T_{htf,out}[K]$	$\Delta T_{htf}[K]$	$\Delta P_{htf}[Pa]$	$Q_{htf,bio}[W]$	$Q_{amb}[W]$
$No\ baffles$	1'127.11	96.037	27.2	9'227.42	430.18
20 mm	1'039.25	183.9	220.8	17'849.34	406.26
10 mm	986.21	236.94	1'563.2	23'097.69	394.11

Table 5.3: Layout comparison: outlet parameters

These initial results require particular attention. As anticipated, the introduction of baffles has a significant impact on the heat transfer rate between the heat transfer fluid and the reactants sides. Table 5.3 shows that the thermal power increases significantly with the introduction of baffles and a reduction in the radial gap. Specifically, the introduction of the first type of baffles results in an absolute thermal power increase of $8'621\ W$, from the initial value of $9'227.42\ W$, representing a 48.30 % increase in the thermal power exchanged between the two sides with a 20 mm air gap. Furthermore, the introduction of baffles with a 10 mm air gap results in a thermal power increase of $13,870.27\ W$, compared to the plain configuration, representing a percentage increase of 150.32 %. These results highlight the crucial role of baffles in enhancing turbulence in the heat transfer fluid flow to increase the convective heat transfer and to provide adequate heat to the reactions occurring in the reactants side. On the other hand, it is clear that as the thermal power exchanged with the reactants side increases, the superheated vapor outlet temperature decreases significantly, resulting in a better utilization of the heat generated by the solar tower. The heat flux through the outer reformer tube is presented in the following figures to provide a clearer understanding. The impact of baffles on the heat flux through the outer reformer tube surface is evident. Figure 5.4 (b) clearly shows a rapid increase in the heat flux downstream of the baffles, where the radial gap is 10 mm. In contrast, for the other geometry, the heat flux increases downstream of the baffles but in a less significant manner. Another important thing that has to be noticed is related to the thermal power exchanged with ambient, as reported in Table 5.3. The thermal losses decreases by introducing baffles mainly because of the lower temperature of the heat transfer fluid flow. On the other hand the thermal power loss through the shell is really small with respect to, for example, the one exchanged inside the reformer, being a small percentage of it. Table 5.3 reveals an important observation regarding the introduction of baffles: the pressure drop increases, particularly when the radial gap is smaller. For instance, the pressure drop increases from 27.2 Pa in the plain configuration to 220.8 Pa for the configuration with 20 mm radial gap baffles, and further increases to $1'563.2$ Pa for the configuration with 10 mm radial gap baffles. Although both the absolute

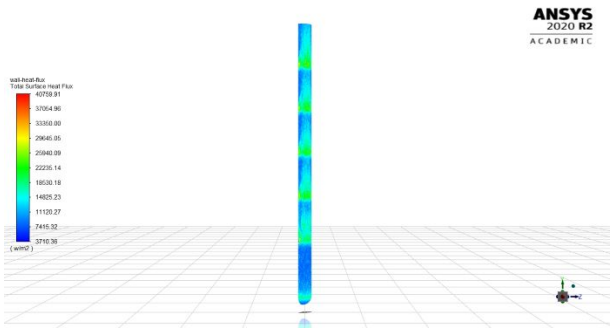

(a) 20 mm baffles configuration.

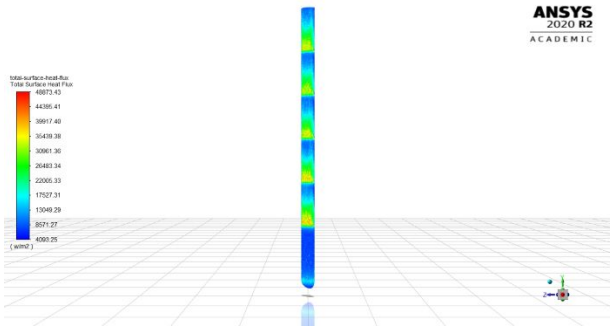

(b) 10 mm baffles configuration.

Figure 5.4: Layout comparison: heat flux

and relative increases in pressure drop due to the introduction of baffles are significant, it is worth noting that the operating pressure of the heat transfer fluid is 101′325 Pa. Thus, the pressure drop caused by the presence of baffles is relatively small compared to the operating pressure. However, the major drawback of introducing baffles is that the pressure drop imposed could be too large depending on the constraints of the reformer plant. In Figures 5.5 and 5.6, differences in generated turbulence can be observed between the two geometries utilizing baffles. The configuration employing baffles with a smaller radial gap produces more effective turbulence. However, it is also evident that the shape of the turbulent profile generated is different due to the difference in radial gap. The first profile is thicker and more uniform on the heat transfer side, while the second profile is steeper and closer to the outer reformer tube. When comparing the turbulent kinetic energy generated downstream of the first and fifth baffles, considering one configuration at time, the shape is similar but differs in magnitude. It is important to underline that there is a significant difference in the flow velocity between the two configurations. Downstream of the first baffle, the flow moves with a maximum velocity of nearly 65 $\frac{m}{s}$ in the configuration with a smaller radial gap. In contrast, with a larger radial gap, the velocity is much lower, with a maximum magnitude of 30 $\frac{m}{s}$. This disparity results in a significantly lower convective heat transfer coefficient, as shown by the global

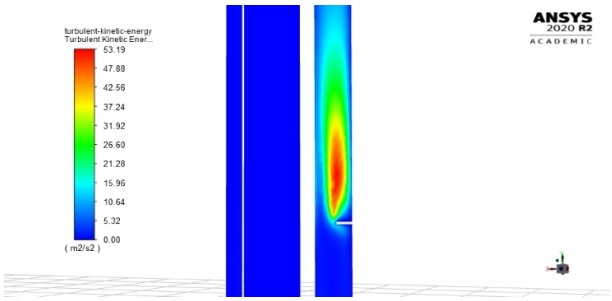

(a) 20 mm baffles.

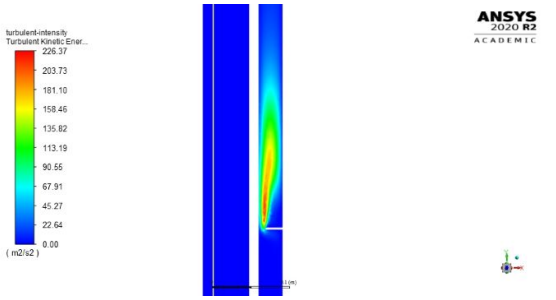

(b) 10 mm baffles.

Figure 5.5: Layout comparison: turbulence $1^{st} baffle$

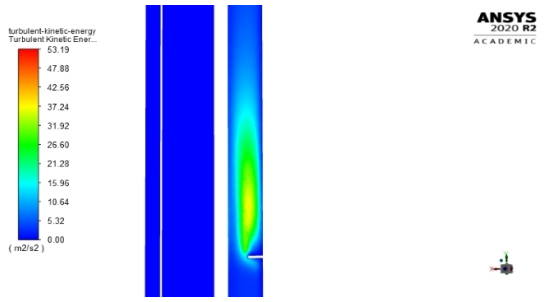

(a) 20 mm baffles.

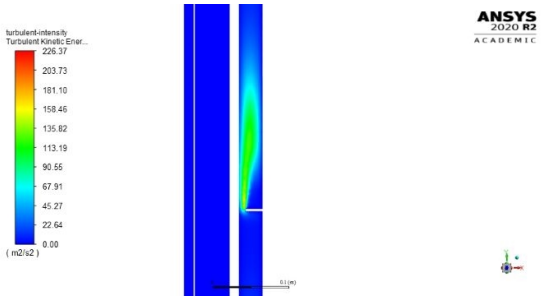

(b) 10 mm baffles.

Figure 5.6: Layout comparison: turbulence $5^{th} baffle$

thermal power exchanged and the heat flux at the outer reformer tube wall.

5.4. Final results

In this section, the final results of the simulations, carried out in ANSYS Fluent, on the bayonet-tube reformer, will be presented. The section is divided in three parts. In the first part, the results on the geometry that presents baffles with radial gap of 20 mm are presented, whereas in the second subsection, the geometry studied presents baffles with radial gap of 10 mm and its behaviour will be highlighted. In the last part, a final comparison between the two considered geometry will be carried out. In both the simulations, the contribution of radiation is considered, in order to model in a realistic way the problem. It is necessary to underline that both the geometries are discretized with similar meshes, in particular the intermediate mesh, as presented in the first section of this chapter, is adopted, because the radiative heat transfer equations require large computational power and by adopting the finest mesh, the simulation time would have been prohibitive.

5.4.1. Case 1: final results

The final results of the CFD simulations on the reformer configuration which presents baffles with 20 mm of radial gap, will be here discussed. The reformer will be analyzed in its totality considering both the heat transfer fluid and the reactants domain, evaluating the heat transfer rates, considering the conversion of the reactants and the quality of the produced syngas. Initially it is important to focus on the main inlet and outlet variables that characterize the fluids processed in the reactor (Table 5.4).

	$\dot{m}[\frac{g}{s}]$	$T_{in}[K]$	$T_{out}[K]$	$\Delta T[K]$	$\Delta P[Pa]$
Steam	42.1800	1'223.15	928.76	294.39	207
Biogas	14.7474	773.15	890.15	117	39'715.5

Table 5.4: Case 1: outlet parameters

First of all it is important to underline that the steam mass flow rate is roughly three times larger than the mass flow rate of biogas. In the biogas side the pressure drop is important and it is due mainly to the deviation that is imposed to the flow in the bottom part of the reformer tube. Considering that biogas enters the reformer at a pressure equal to 10 bar, the pressure drop accounts for 1% of the inlet pressure of the flow. The

pressure drop in the superheated steam side is, in contrary, much lower and, as already explained, mainly due to the restriction imposed by the baffles. For what regards the outlet temperature and the temperature difference between inlet and outlet, some aspects need to be clarified. The temperature decrease of the superheated steam flow is lower with respect to the temperature increase in the biogas flow, even if the mass flow rate of the latter is much lower. In order to explain this aspect, it is necessary to recall that, as will be shown, most of the thermal power exchanged between the two flows is adopted in order to feed the endothermic reactions occurring in the biogas side. Furthermore, the already reacted syngas, which is at an higher temperature with respect to the biogas, exchanges heat with the biogas side, decreasing in this way its outer temperature. In order to have a more clear idea of what happens inside the reformer unit, the thermal power exchanged inside it, must be shown (Table 5.5).

$Q_{htf,bio}[W]$	$Q_{sensible}[W]$	$Q_{reaction}[W]$	$Q_{recovered}[W]$	$Q_{htf,amb}[W]$
29'108.64	5'370.63	23'737.98	3'523.764	336.39

Table 5.5: Case 1: reformer heat transfer

Considering the whole thermal power exchanged between the two flows, clearly going from the superheated steam to the biogas, only a minor part of it is used to increase the temperature of the reactants flow (18.45%), while the largest portion is necessary in order to carry out the reforming reactions inside the reformer (81.55%). The thermal power exchanged through the shell, between the steam and the environment, is small with respect to the heat actually released to the biogas flow. The last quantity presented in Table 5.5 indicates the thermal power that is exchanged between the syngas and the biogas, that is the portion of heat recovered thanks to the adoption of a bayonet-tube configuration. This quantity is important, in fact accounts for 12% of the heat released by the superheated steam to the reactants side. Lastly, by comparing the thermal power exchanged between the steam and the biogas when radiation is considered (Table 5.5) and when it is neglected (Table 5.3), it is possible to evaluate the impact of radiation. In particular, the thermal power increases from $17'849.34\ W$ up to $29'108.64\ W$, which means that radiative heat transfer imposes a percentage increase in the thermal power exchanged equal to 63%. Both the biogas inlet and the syngas outlet compositions are shown in table 5.6.

	X_{CH4}	X_{H2}	X_{CO}	X_{CO2}	X_{H2O}	X_{N2}
Inlet	0.2470	0	0	0.2221	0.4929	0.0380
Outlet	0.0451	0.4068	0.1335	0.1638	0.2230	0.0278

Table 5.6: Case 1: syngas composition

Before evaluating the process and biogas quality, it is fundamental to recall that the reactions have been carried out considering the thermodynamic equilibrium composition. The conversion of methane (CH_4) is defined as follows:

$$\chi_{\mathrm{CH_4}} = \frac{\dot{n}_{\mathrm{CH_4},in} - \dot{n}_{\mathrm{CH_4},out}}{\dot{n}_{\mathrm{CH_4},in}}$$

The methane conversion in this configuration is equal to 75%. On the other hand, the H_2/CO of the syngas is similar to 3.

5.4.2. Case 2: final results

The final results of the CFD simulations on the reformer configuration which presents baffles with 10 mm of radial gap, will be here discussed. The first aspects that need to be underlined, are the outlet parameter of the two fluid flows in the reformer unit.

	$\dot{m}[\frac{g}{s}]$	$T_{in}[K]$	$T_{out}[K]$	$\Delta T[K]$	$\Delta P[Pa]$
Steam	42.1800	1'223.15	906.11	317.04	1'454.6
Biogas	14.7474	773.15	896.82	123.67	40'570

Table 5.7: Case 2: outlet parameters

The mass flow rates processed in the reformer are equal to the one considered in case 1. The pressure drop in the heat transfer fluid domain is high due to the small axial section made available by the baffles. The heat transfer properties of the reformer are highlighted in the following table.

$Q_{htf,bio}[W]$	$Q_{sensible}[W]$	$Q_{reaction}[W]$	$Q_{recovered}[W]$	$Q_{htf,amb}[W]$
31'271.52	5'713.815	25'557.7	3'719.7	337.53

Table 5.8: Case 2: reformer heat transfer

Considering the total thermal power exchanged between the two fluids, only a small portion of it is used to heat up the biogas flow, which accounts for 18.27% of the total power, whereas the largest portion allows the endothermic reactions to proceed towards the desired direction (71.73% of the total). The heat exchanged with the environment through the shell are minimum and does not represent an important loss in the overall process. It is important to further underline that the thermal power recovered thanks to the bayonet-tube configuration is important if compared to the heat exchanged between the steam and biogas sides, representing an addition equal to the 11.89% of the total. By making the same consideration as in case 1, it is important to underline that the increase in the thermal power between the steam and biogas sides, due to the radiative contribution, is equal to $8'173.83\ W$, which, considering that without radiation the total value is $23'097.69\ W$, represents a percentage increase of 36%. The last considerations need to be done about the outlet composition of the produced syngas.

	X_{CH4}	X_{H2}	X_{CO}	X_{CO2}	X_{H2O}	X_{N2}
Inlet	0.2470	0	0	0.2221	0.4929	0.0380
Outlet	0.0358	0.4201	0.1452	0.1556	0.2161	0.0273

Table 5.9: Case 2: syngas composition

The methane conversion is equal to 80% while the H_2/CO is equal to 2.9.

5.4.3. Reformer layout comparison

A comparison between the two configuration considered in the last sections is necessary in order to understand what kind of baffles adopt in order to achieve better reformer properties. The main aspects that has to be considered is the heat transfer characteristics of the processes in the two different cases. Comparing the values of thermal power exchanged between the steam and biogas sides in the two configurations, reported in table 5.5 and 5.8 respectively for case 1 and case 2, it is evident that the heat transfer is larger in the configuration that adopts the baffles with the smaller radial gap. In particular, for case 1, the thermal power exchanged between the two flows is equal to $29'108.64\ W$ whereas, for case 2, it amounts to $31'271.52\ W$, which is 7.43% of increase. This effect is due to the higher turbulence that is generated by the baffles, because, by imposing a smaller axial section to the flow, an higher turbulence and an higher velocity are generated, which results in higher convective heat transfer. It is possible to see the different in the heat flux through the outer reformer tube between the two configurations. It is clear that in

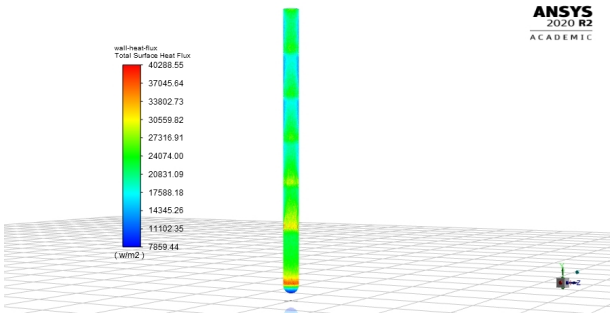

(a) Case 1.

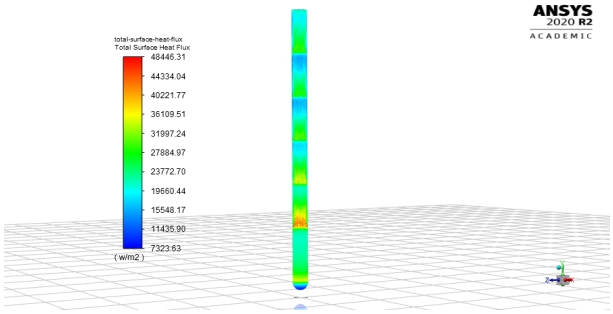

(b) Case 2.

Figure 5.7: Layout comparison: heat flux outer reformer tube

the configuration of case 2, the heat flux is strongly increased downstream the baffles, in particular downstream the first baffle. A key aspect that has to be underlined is related with the really low heat flux through the bottom part of the bayonet-tube, that can be seen in both configurations, highlighted in figure 2.8. This poor heat transfer is due to the low velocity of the syngas near the wall in the bottom part of the bayonet-tube. In particular, the flow, near the bottom part of the tube, shows a velocity near to zero even far from the wall. This dead zone is related to the shape of the tube. Considering the syngas production, it is fundamental to underline that the configuration of case 2 allows to have higher conversion of methane (CH_4), which is an important parameter to consider in a reforming process, while the syngas are characterized by a similar H_2/CO ratio. This fact is due mainly to an higher production both of H_2 and CO, which means, a syngas composed in a larger part of the two desired product. In conclusion, the geometry that presents baffles with a smaller radial gap, allows to produce syngas of an higher quality due to the better heat transfer properties guaranteed by the spider baffles. On the other hand, as already underlined, the higher pressure drop imposed in the steam domain, due to smaller available axial section in proximity of the baffles, can represent a limitation.

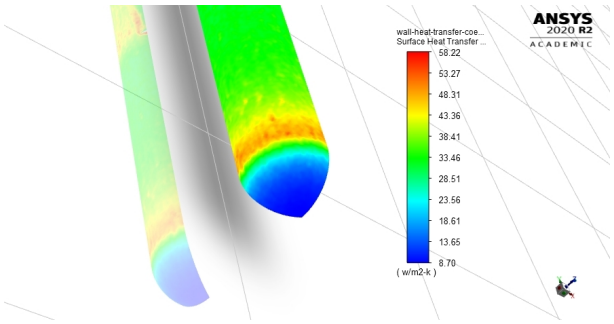

(a) Case 1.

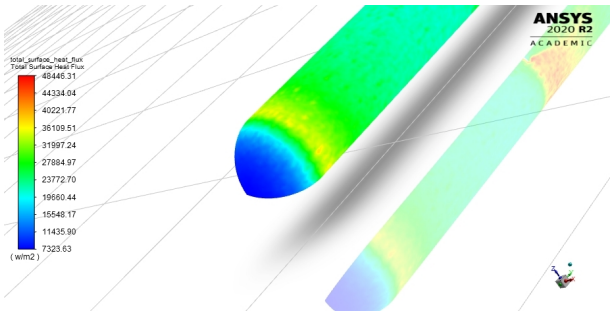

(b) Case 2.

Figure 5.8: Layout comparison: heat flux bottom part reformer tube

6 | Conclusions and outlook

This thesis work stems from the need to find a way to increase the heat exchange between the fluid and the reactants in a heat exchange reformer with bayonet geometry. In a previous study, in fact, the convective heat exchange properties inside the reformer were found to be insufficient to properly feed the reactions proper to the process. With the aim of improving this limiting aspect of the reformer, spider baffles were introduced to increase the turbulence and consequently, the convective heat transfer properties of the reformer under study. The results obtained and shown in the dedicated chapter, demonstrate that the introduction of such baffles is extremely beneficial to the reformer, bringing major advantages and minor disadvantages. As has been demonstrated, the introduction of baffles considerably increases the convective heat exchange within the reformer, hitting what was the aim of the study. By comparing two geometries with slightly different characteristics, it was also possible to show what benefits and disadvantages the reduction of the radial gap of spider baffles brings. In particular, it was shown that a decrease in the above-mentioned characteristic makes it possible to increase turbulence and convective heat exchange inside the reactor, at the expense of a greater pressure drop, linked to the narrowing of the passage section imposed by the baffles themselves. For this reason, it was evident that the decrease in this parameter is generally positive, depending, however, on the limits imposed by the process of which the reactor will be a part. The project is still at an early stage and therefore full of possible and necessary future developments. With the aim of creating a model that is more faithful to reality, it is certainly necessary to study the chemistry of the process in greater detail. In particular, evaluating the development of reactions in contact with the catalyst is a step that must be taken, accompanied by greater care in using models that consider the actual kinetics of reforming reactions. In any case, the reformer is correctly designed and has, potentially and depending on economic evaluations to be made downstream of the modelling, great potential as it fits into a context that needs innovation and moves in an environmentally sustainable direction, an aspect that undoubtedly remains a priority in the industrial sector.

Bibliography

[1] Per Tuna. *Generation of synthesis gas for fuels and chemicals production*. Department of Chemical Engineering, Lund University, 2013. ISBN 9789174223217.

[2] D. Prato-Garcia, A. Robayo-Avendaño, and R. Vasquez-Medrano. Hydrogen from natural gas and biogas: Building bridges for a sustainable transition to a green economy. *Gas Science and Engineering*, 111:204918, 3 2023.

[3] Rayssa Luana da Silva Pinto, Alexia Coelho Vieira, Aline Scarpetta, Felipe Souza Marques, Regina Maria Matos Jorge, Alesandro Bail, Luiz Mario Matos Jorge, Marcos Lúcio Corazza, and Luiz Pereira Ramos. An overview on the production of synthetic fuels from biogas. *Bioresource Technology Reports*, 18, 6 2022.

[4] Shanshan Lu, Yanmei Shi, Nannan Meng, Siyu Lu, Yifu Yu, and Bin Zhang. Electrosynthesis of syngas via the co-reduction of co2 and h2o. *Cell Reports Physical Science*, 1, 11 2020.

[5] P. Samuel. Gtl technology challenges and opportunities in catalysis. *Bulletin of the Catalysis Society of India*, pages 82–99, 2003.

[6] P. Chiesa. *15 - Advanced technologies for syngas and hydrogen (H2) production from fossil-fuel feedstocks in power plants*. Elsevier Inc., 2010.

[7] Paloma Ferreira-Aparicio, M. J. Benito, and J. L. Sanz. New trends in reforming technologies: From hydrogen industrial plants to multifuel microreformers. *Catalysis Reviews - Science and Engineering*, 47:491–588, 2005.

[8] Jakob S. Engbaek, Søren B. Vendelbo, Flemming B. Bendixen, Winnie L. Eriksen, Kim Aasberg-Petersen, Ib Chorkendorff Cathrine Frandsen, and Peter M. Mortensen Sebastian T. Wismann. Electrified methane reforming: A compact approach to greener industrial hydrogen production. *Science 364*, pages 756–759, 2019.

[9] JR Rostrupnielsen and JH Bak Hansen. Co2-reforming of methane over transition metals. *Journal of Catalysis*, 144(1):38–49, 1993.

[10] K. Aasberg-Petersen, I. Dybkjær, C. V. Ovesen, N. C. Schjødt, J. Sehested, and S. G.

Thomsen. Natural gas to synthesis gas - catalysts and catalytic processes. *Journal of Natural Gas Science and Engineering*, 3:423–459, 5 2011.

[11] Adewale George Adeniyi, Kevin Shegun Otoikhian, and Joshua O. Ighalo. Steam reforming of biomass pyrolysis oil a review. *International Journal of Chemical Reactor Engineering*, 17(4):20180328, 2019.

[12] S. Hafeez, E. Pallari, G. Manos, and A. Constantinou. Catalytic conversion and chemical recovery. pages 147–172, 2018.

[13] Naiara García-Gómez, Beatriz Valle, José Valecillos, Aingeru Remiro, Javier Bilbao, and Ana G. Gayubo. Feasibility of online pre-reforming step with dolomite for improving ni spinel catalyst stability in the steam reforming of raw bio-oil. *Fuel Processing Technology*, 215, 5 2021.

[14] Velu Subramani, Angelo Basile, and T Nejat Veziroglu. *Compendium of hydrogen energy Hydrogen production and purification*. Elsevier Science, 2015.

[15] Salwa A. Ghoneim, Radwa A. El-Salamony, and Seham A. El-Temtamy. Review on innovative catalytic reforming of natural gas to syngas. *World Journal of Engineering and Technology*, 04:116–139, 2016.

[16] Lois Milner-Elkharouf, Martin Khzouz, and Robert Steinberger-Wilckens. Catalyst development for indirect internal reforming (iir) of methane by partial oxidation. *International Journal of Hydrogen Energy*, 45:5285–5296, 2 2020.

[17] David Rennard, Rick French, Stefan Czernik, Tyler Josephson, and Lanny Schmidt. Production of synthesis gas by partial oxidation and steam reforming of biomass pyrolysis oils. *International Journal of Hydrogen Energy*, 35:4048–4059, 5 2010.

[18] R.L. Keiski, S. Ojala, M. Huuhtanen, T. Kolli, and K. Leiviskä. *9 - Partial oxidation (POX) processes and technology for clean fuel and chemical production*. Woodhead Publishing Series in Energy. Woodhead Publishing, 2011.

[19] L.S. Neiva. A study on the characteristics of the reforming of methane: A review. *Brazilian Journal of Petroleum and Gas*, pages 119–127, 9 2010. ISSN 19820593. doi: 10.5419/bjpg2010-0013.

[20] F. M.H., Owrand and J.E Rafiq Hustad. Synthesis gas from methane by using plasma-assisted gliding arc catalytic partial oxidation reactor. *1st Trondheim Gas Technology Conference*, pages 1667–1670, 10 2009.

[21] J.A Liu. Kinetics, catalysis and mechanism of methane steam reforming. 2006.

[22] Gianluca Pauletto, Nicole Libretto, Daria C. Boffito, Jeffrey T. Miller, Andreas Jentys, Gregory S. Patience, and Johannes A. Lercher. Ni/ceo2 promoted ru and pt supported on fecral gauze for cycling methane catalytic partial oxidation—cpox. *Applied Catalysis B: Environmental*, 286, 6 2021.

[23] L Basini, K Aasberg-Petersen, A Guarinoni, M Østberg, and Snamprogetti SpA. Catalytic partial oxidation of natural gas at elevated pressure and low residence time. *Catalysis Today*, 64:9–20, 2001.

[24] Halit Eren Figen and Sema Z. Baykara. Effect of ruthenium addition on molybdenum catalysts for syngas production via catalytic partial oxidation of methane in a monolithic reactor. *International Journal of Hydrogen Energy*, 43:1129–1138, 2018.

[25] Amir Mosayebi. Kinetic modeling of catalytic partial oxidation of methane over ni-rh/*gamma*-al2o3 catalyst for syngas formation. *Journal of the Taiwan Institute of Chemical Engineers*, 114:36–46, 9 2020.

[26] A S Bodke, S S Bharadwaj, and L D Schmidt. The effect of ceramic supports on partial oxidation of hydrocarbons over noble metal coated monoliths 1. *JOURNAL OF CATALYSIS*, 179:138–149, 1998.

[27] P. Arku, B. Regmi, and A. Dutta. A review of catalytic partial oxidation of fossil fuels and biofuels: Recent advances in catalyst development and kinetic modelling. *Chemical Engineering Research and Design*, 136:385–402, 8 2018.

[28] José Juan Bolívar Caballero, Ilman Nuran Zaini, and Weihong Yang. Reforming processes for syngas production: A mini-review on the current status, challenges, and prospects for biomass conversion to fuels. *Applications in Energy and Combustion Science*, 10, 6 2022.

[29] K Aasberg-Petersen, J.-H Bak Hansen, T S Christensen, I Dybkjaer, P Seier Christensen, C Stub Nielsen, S E L Winter Madsen, and J R Rostrup-Nielsen. Technologies for large-scale gas conversion. *Applied Catalysis A: General*, 221:379–387, 2001.

[30] Mathilde Luneau, Elia Gianotti, Frédéric C. Meunier, Claude Mirodatos, Eric Puzenat, Yves Schuurman, and Nolven Guilhaume. Deactivation mechanism of ni supported on mg-al spinel during autothermal reforming of model biogas. *Applied Catalysis B: Environmental*, 203:289–299, 4 2017.

[31] Y. S. Montenegro Camacho, S. Bensaid, G. Piras, M. Antonini, and D. Fino. Techno-economic analysis of green hydrogen production from biogas autothermal reforming. *Clean Technologies and Environmental Policy*, 19:1437–1447, 7 2017.

[32] R. Y. Chein, Y. C. Chen, C. T. Yu, and J. N. Chung. Thermodynamic analysis of dry reforming of ch4 with co2 at high pressures. *Journal of Natural Gas Science and Engineering*, 26:617–629, 9 2015.

[33] Hale Akansu, Huseyin Arbag, H. Mehmet Tasdemir, Sena Yasyerli, Nail Yasyerli, and Gulsen Dogu. Nickel-based alumina supported catalysts for dry reforming of biogas in the absence and the presence of h2s: Effect of manganese incorporation. *Catalysis Today*, 397-399:37–49, 8 2022.

[34] Bawadi Abdullah, Nur Azeanni Abd Ghani, and Dai Viet N. Vo. Recent advances in dry reforming of methane over ni-based catalysts. *Journal of Cleaner Production*, 162:170–185, 9 2017.

[35] Zhaoyin Hou, Ping Chen, Heliang Fang, Xiaoming Zheng, and Tatsuaki Yashima. Production of synthesis gas via methane reforming with co2 on noble metals and small amount of noble-(rh-) promoted ni catalysts. *International Journal of Hydrogen Energy*, 31:555–561, 4 2006.

[36] Adolfo E. Castro Luna and María E. Iriarte. Carbon dioxide reforming of methane over a metal modified ni-al2o3 catalyst. *Applied Catalysis A: General*, 343:10–15, 7 2008.

[37] Yasotha Kathiraser, Usman Oemar, Eng Toon Saw, Ziwei Li, and Sibudjing Kawi. Kinetic and mechanistic aspects for co2 reforming of methane over ni based catalysts. *Chemical Engineering Journal*, 278:62–78, 6 2015.

[38] Reiyu Chein and Zeng Wei Yang. H2s effect on dry reforming of biogas for syngas production. *International Journal of Energy Research*, 43:3330–3345, 6 2019.

[39] Abdollah Hajizadeh, Mohamad Mohamadi-Baghmolaei, Noori M. Cata Saady, and Sohrab Zendehboudi. Hydrogen production from biomass through integration of anaerobic digestion and biogas dry reforming. *Applied Energy*, 309, 3 2022.

[40] Weizuo Li, Zhongkui Zhao, Fanshu Ding, Xinwen Guo, and Guiru Wang. Syngas production via steam-co2 dual reforming of methane over la-ni/zro2 catalyst prepared by l -arginine ligand-assisted strategy: Enhanced activity and stability. *ACS Sustainable Chemistry and Engineering*, 3:3461–3476, 10 2015.

[41] Monica Dan, Maria Mihet, and Mihaela D. Lazar. Hydrogen and/or syngas production by combined steam and dry reforming of methane on nickel catalysts. *International Journal of Hydrogen Energy*, 45:26254–26264, 10 2020.

[42] G. Mallikarjun, T. V. Sagar, S. Swapna, N. Raju, P. Chandrashekar, and N. Linga-

iah. Hydrogen rich syngas production by bi-reforming of methane with co2over ni supported on ceo2-sro mixed oxide catalysts. *Catalysis Today*, 356:597–603, 10 2020.

[43] I. P. Moura, A. C. Reis, A. E. Bresciani, and R. M.B. Alves. Carbon dioxide abatement by integration of methane bi-reforming process with ammonia and urea synthesis. *Renewable and Sustainable Energy Reviews*, 151, 11 2021.

[44] Florent Minette and Juray De Wilde. Multi-scale modeling and simulation of low-pressure methane bi-reforming using structured catalytic reactors. *Chemical Engineering Journal*, 407, 3 2021.

[45] Mohammad Osat and Faryar Shojaati. Assessing performance of methane tri-reforming reactor using a parametric study on the fundamental process variables. *Cleaner Chemical Engineering*, 3:100050, 9 2022.

[46] Rajib Kumar Singha, Astha Shukla, Aditya Yadav, Shubhadeep Adak, Zafar Iqbal, Nazia Siddiqui, and Rajaram Bal. Energy efficient methane tri-reforming for synthesis gas production over highly coke resistant nanocrystalline ni-zro2 catalyst. *Applied Energy*, 178:110–125, 9 2016.

[47] Santiago Veiga, Ricardo Faccio, Mariano Romero, and Juan Bussi. Nilam (m = ce and/or zr) mixed oxide catalysts for synthesis gas production by biogas reforming processes. *Materials Letters*, 293, 6 2021.

[48] Mohammad Hasan Khademi, Afshar Alipour-Dehkordi, and Masoud Tabesh. Optimal design of methane tri-reforming reactor to produce proper syngas for fischer-tropsch and methanol synthesis processes: A comparative analysis between different side-feeding strategies. *International Journal of Hydrogen Energy*, 46:14441–14454, 4 2021.

[49] K. Świrk, J. Grams, M. Motak, P. Da Costa, and T. Grzybek. Understanding of tri-reforming of methane over ni/mg/al hydrotalcite-derived catalyst for co2utilization from flue gases from natural gas-fired power plants. *Journal of CO2 Utilization*, 42, 2020.

[50] Yong Ho Yu and Mihail H Sosna. Modeling for industrial heat exchanger type steam reformer. *Koreano r. Chem. Eng*, 18:127–132, 2001.

[51] *ANSYS Fluent Theory Guide*.

[52] Brian Launder, B E Launder, and B I Sharma. Application of the energy-dissipation model of flow near a spinning disc using engineering cfd techniques to improve hurrican predictions, especially the air-sea interface and sea beneath. view project ac-

curate spectral collocation methods for navier stokes solvers cnrs ccvr view project. *LETTERS IN HEAT AND MASS TRANSFER*, I:131–138, 1974.

[53] Brian Launder, B E Launder, and D B Spalding. The numerical computation of turbulent flows using engineering cfd techniques to improve hurrican predictions, especially the air-sea interface and sea beneath. view project accurate spectral collocation methods for navier stokes solvers cnrs ccvr view project the numerical computation of turbulent flows. *COMPUTER METHODS IN APPLIED MECHANICS ANR ENGINEERING*, 3:269–289, 1974.

[54] Brian Launder. The prediction of laminarization with a two-equation model of turbulence, " using engineering cfd techniques to improve hurrican predictions, especially the air-sea interface and sea beneath. view project accurate spectral collocation methods for navier stokes solvers cnrs ccvr view project, 2016. URL `https://www.researchgate.net/publication/313117966`.

[55] Tsan-Hsing Shih, William W Liou, Aamir Shabbir, Zhigang Yang, and Jiang Zhu. A new kt eddy viscosity model for high :reynolds number turbulent flows. *Compurers Fluids*, 24:227–238, 1995.

[56] Fluid mechanics 101.

List of Figures

List of Tables

List of Symbols

Variable	Description	SI unit
ρ	density	$\frac{kg}{m^3}$
$\boldsymbol{U}$	velocity vector	$\frac{m}{s}$
U_i	scalar velocity in i-direction	$\frac{m}{s}$
D_ϕ	Diffusivity of quantity ϕ	$\frac{m^2}{s}$
∇	nabla operator	$[-]$
$\overline{\overline{\tau}}$	stress tensor	$[-]$
e	Internal energy	$\frac{m^2}{s^2}$
h	enthalpy	$\frac{m^2}{s^2}$
Y_j	mass fraction of j^{th}	[-]
M_j	molecular mass of j^{th} species	$\frac{kg}{kmol}$
k	thermal conductivity	$\frac{W}{m^2K}$
σ	Stefan boltzmann constant	$\frac{W}{m^2K^4}$
I	intensity of radiation	$\frac{W}{sr}$
$\boldsymbol{r}$	position vector	m
$\boldsymbol{s}$	directional vector	$[-]$
a	absorption coefficient	$[-]$
σ_s	scattering coefficient	$[-]$
n	refractive index	$[-]$
Φ	phase function	$[-]$
Ω	solid angle	$[-]$
μ	dynamic viscosity	$kg\frac{m}{s}$
k	turbulent kinetic energy	$\frac{m^2}{s^2}$
ϵ	turbulence dissipation rate	$\frac{m^2}{s^2}$
μ_t	turbulent viscosity	$kg\frac{m}{s}$
ω	specific turbulent dissipation rate	$\frac{m^2}{s^3}$